

GFPT2/GFAT2 and AMDHD2 act in tandem to control the hexosamine pathway.

Virginia Kroef^{1*}, Sabine Ruegenberg^{1,2*}, Moritz Horn^{1,3}, Kira Allmeroth¹, Lena Ebert^{4,5,6}, Seyma Bozkus², Stephan Miethel¹, Ulrich Elling⁷, Bernhard Schermer^{4,5,6}, Ulrich Baumann², Martin S. Denzel^{1,5,6}

¹Max Planck Institute for Biology of Ageing
D-50931 Cologne, Germany

²Institute of Biochemistry
University of Cologne
D-50674 Cologne, Germany

³JLP Health GmbH
A-1130 Vienna, Austria and
Acus Laboratories GmbH
D-50931 Cologne, Germany

⁴Department II of Internal Medicine
University of Cologne
Faculty of Medicine and University Hospital Cologne
D-50931 Cologne, Germany

⁵Center for Molecular Medicine Cologne (CMMC)
Faculty of Medicine and University Hospital Cologne
University of Cologne
D-50931 Cologne, Germany

⁶CECAD - Cluster of Excellence
Faculty of Medicine and University Hospital Cologne
University of Cologne
D-50931 Cologne, Germany

⁷IMBA - Institute of Molecular Biotechnology of the Austrian Academy of Science
Vienna Biocenter
A-1030 Vienna, Austria

*These authors contributed equally

correspondence:

mdenzel@age.mpg.de

Abstract

The hexosamine biosynthetic pathway (HBP) produces the essential metabolite UDP-GlcNAc and plays a key role in metabolism, health, and aging. The HBP is controlled by its rate-limiting enzyme glutamine fructose-6-phosphate amidotransferase (GFPT/GFAT) that is directly inhibited by UDP-GlcNAc in a feedback loop. HBP regulation by GFPT is well studied but other HBP regulators have remained obscure. Elevated UDP-GlcNAc levels counteract the glycosylation toxin tunicamycin (TM) and thus we screened for TM resistance in haploid mouse embryonic stem cells (mESCs) using random chemical mutagenesis to determine alternative HBP regulation. We identified the N-acetylglucosamine deacetylase AMDHD2 that catalyzes a reverse reaction in the HBP and its loss strongly elevated UDP-GlcNAc. To better understand AMDHD2, we solved the crystal structure and found that loss-of-function is caused by protein destabilization or interference with its catalytic activity. Finally, we show that mESCs express AMDHD2 together with GFPT2 instead of the more common paralog GFPT1. Compared with GFPT1, GFPT2 had a much lower sensitivity to UDP-GlcNAc inhibition, explaining how AMDHD2 loss-of-function resulted in HBP activation. This HBP configuration in which AMDHD2 serves to balance GFPT2 activity was also observed in other mESCs and, consistently, the GFPT2:GFPT1 ratio decreased with differentiation of human embryonic stem cells. Together, our data reveal a critical function of AMDHD2 in limiting UDP-GlcNAc production in cells that use GFPT2 for metabolite entry into the HBP.

Introduction

The hexosamine biosynthetic pathway (HBP) is an anabolic branch of glycolysis consuming about 2-3% of cellular glucose^{1,2}. It provides substrates for various posttranslational modification (PTM) reactions and has been strongly associated with stress resistance and longevity as well as cell growth and transformation³⁻⁵. Thus, the HBP plays an essential role for metabolic adaptations and cellular homeostasis⁶.

In the first and rate limiting step of the HBP, glutamine fructose-6-phosphate amidotransferase (GFPT) converts fructose-6-phosphate (Frc6P) and L-glutamine (L-Gln) to D-glucosamine-6-phosphate (GlcN6P)². The two mammalian GFPT paralogs GFPT1 and GFPT2 show 75-80% amino acid sequence identity⁷. While GFPT1 is ubiquitously expressed, GFPT2 is reported to be predominantly expressed in the nervous system. Notably, GlcN6P can be converted to Frc6P by glucosamine-6-phosphate deaminase 1 and 2 (GNPDA1/2), shunting metabolites back into glycolysis⁸. In the second step of the HBP, glucosamine-phosphate N-acetyltransferase (GNA1) acetylates GlcN6P to N-acetylglucosamine-6-phosphate (GlcNAc-6P) using acetyl-CoA as the acetyl donor⁹. This reaction is also presumed to be reversible through deacetylation of GlcNAc6P^{10,11}. After isomerization into GlcNAc-1-phosphate (GlcNAc-1P) mediated by GlcNAc phosphomutase (PGM3), UTP is used in a final step by UDP-N-acetylglucosamine pyrophosphorylase (UAP1) to synthesize the final product uridine 5'-diphosphate-N-acetyl-D-glucosamine (UDP-GlcNAc)^{12,13}. UDP-GlcNAc can be reversibly interconverted to its epimer uridine 5'-diphosphate-N-acetyl-D-galactosamine (UDP-GalNAc) by the enzyme UDP-galactose-4'-epimerase (GALE) and the pool of both metabolites is termed

UDP-HexNAc¹⁴. The HBP is the only source for UDP-GlcNAc and relies on substrates from carbon, nitrogen, fatty-acid, and energy metabolism. It is therefore optimally positioned as a metabolic sensor that can modulate downstream cellular signaling through UDP-GlcNAc dependent PTMs¹.

UDP-GlcNAc is a precursor of several important biomolecules such as chitin, peptidoglycans, glycosaminoglycans, and for a number of dynamic glycosylation events. Mucin-type O-glycosylation plays an important role in the extracellular matrix¹⁵. N-linked-glycosylation orchestrates protein folding in the endoplasmic reticulum (ER) and is therefore crucial in protein homeostasis¹⁶. N-glycans further contribute to the cell surface glycocalyx as structural components of proteins¹⁷. Finally, the addition of single GlcNAc moieties to Thr/Ser residues, termed O-GlcNAcylation, occurs dynamically on hundreds of proteins, thus modulating a variety of downstream pathways¹⁸. Surprisingly, this dynamic PTM is accomplished by a single protein, O-GlcNAc transferase (OGT), and O-GlcNAcase (OGA) is the only known enzyme to remove O-GlcNAc modifications^{19,20}. While it is known that these glycosylation reactions are limited by intracellular UDP-GlcNAc, how the HBP is regulated to adapt UDP-GlcNAc levels according to nutrient availability is poorly understood. Due to the diverse function of UDP-GlcNAc, alterations in its abundance can have detrimental effects resulting in pathological conditions like diabetes, cancer, cardiovascular diseases, and neurodegenerative diseases^{1,21-23}.

In a previous chemical mutagenesis screen in *Caenorhabditis elegans* we isolated mutants resistant to the toxin tunicamycin (TM) as a proxy for enhanced protein quality control and found that TM resistant mutants were enriched for longevity³. TM is a competitive inhibitor of UDP-

GlcNAc:dolichylphosphate GlcNAc-1-phosphotransferase (GPT), which catalyzes the first step of N-glycan synthesis utilizing UDP-GlcNAc²⁴. TM thus disrupts N-glycosylation and leads to proteins misfolding and proteotoxic stress¹⁶. We found that single amino acid substitutions in GFPT1 result in gain-of-function due to loss of UDP-GlcNAc feedback inhibition, elevating cellular UDP-GlcNAc levels and thereby counteracting TM toxicity²⁵. By introducing the same gain-of-function mutation in GFPT1 of mouse neuroblastoma Neuro2a (N2a) cells, we confirmed a conserved mechanism²⁶, suggesting that screening for TM resistance might be a suitable unbiased means to analyze the HBP through genetic approaches in mammalian cells. Based on this knowledge, we aimed to identify novel regulators of the HBP in mammalian cells, which could serve as potential drug targets for future therapeutic interventions.

In this study, we combined chemical mutagenesis with whole exome sequencing in haploid murine cells and identified the N-acetylglucosamine-6-phosphate deacetylase AMDHD2 (Amidohydrolase Domain Containing 2) as a novel regulator of the HBP. Through AMDHD2 deletion, we discovered a configuration of the HBP that uses GFPT2 as the key enzyme. Functionally, GFPT2 shows a lower sensitivity to UDP-GlcNAc feedback inhibition compared to GFPT1 therefore requiring AMDHD2 to balance HBP metabolic flux.

Results

Chemical mutagenesis screen for tunicamycin resistance in haploid mESCs identifies AMDHD2

Elevated HBP activity and high UDP-GlcNAc concentrations suppress TM toxicity, making TM resistance a proxy for HBP activity in genetic screens. To investigate HBP regulation in mammalian cells we therefore performed an unbiased TM resistance screen. The mutagen N-ethyl-N-nitrosourea (ENU) induces single nucleotide variants that enable a screen at amino acid resolution. Thus, we used ENU in haploid cells, which uniquely enable identification of recessive alleles²⁷⁻²⁹. In order to reach a high degree of saturation, 27 million AN3-12 mouse embryonic stem cells (mESCs) were used for mutagenesis. This was followed by TM selection using a WT lethal dose (0.5 µg/ml) for three weeks (Figure 1A). 29 resistant clones were randomly selected and picked to grow isogenic mutant lines. Whole exome sequencing was done with four clones, which showed strong TM resistance (Figure 1-figure supplement 1A). Two clones revealed independent missense mutations in the *Amdhd2* coding sequence (Figure 1-figure supplement 1B). A second round of whole exome sequencing of the remaining 25 clones revealed in total 11 independent amino acid substitutions at 10 distinct positions in *Amdhd2* (38% of sequenced clones) (Figure 1B, Figure 1-figure supplement 1B). Surprisingly we did not identify any mutations in the HBP's rate limiting enzymes *Gfpt1* or *Gfpt2*. In addition, we performed a random insertional mutagenesis screen using an enhanced gene trapping system, which was previously established in haploid mESCs (Figure 1-figure supplement 1C)³⁰. After selection for TM resistance and mapping of the insertion site by Sanger sequencing, we identified *Amdhd2*

in 4 of the 20 analyzed clones (Figure 1C, Figure 1-figure supplement 1C). Since disruption of the *Amdhd2* locus by transgene insertion was sufficient to mediate TM resistance, we concluded that the identified mutations are loss-of-function mutations. To corroborate that *Amdhd2* disruption leads to TM resistance we generated *Amdhd2* KO mutants in diploid WT AN3-12 cells using CRISPR/Cas9. We generated and validated a specific AMDHD2 antibody, which confirmed a successful KO of AMDHD2 (Figure 1D). To exclude off target effects, we generated three independent *Amdhd2* KO lines using distinct guide combinations. All homozygous *Amdhd2* KO cells showed significant TM resistance compared to WT cells, confirming AMDHD2 loss-of-function as causal for TM resistance (Figure 1E,F, Figure 1-figure supplement 1D).

Disruption of *Amdhd2* mediates tunicamycin resistance via elevated HBP flux

AMDHD2 is an amidohydrolase that plays a potential role in the HBP by catalyzing the deacetylation of GlcNAc-6P in the “reverse” direction of the pathway³¹. However, a role of AMDHD2 in modulating cellular UDP-GlcNAc levels has not been recognized before. We hypothesized that AMDHD2 loss-of-function might increase UDP-GlcNAc levels leading to TM resistance (Figure 2A). To test this, we measured UDP-GlcNAc levels via ionic chromatography/mass spectrometry (IC-MS) and found that TM resistant mutants identified in the insertional mutagenesis screen (clone 1-4) as well as the CRISPR/Cas9-generated AMDHD2 KO mutants showed a significant increase in UDP-GlcNAc concentrations (Figure 2B, Figure 2-figure supplement 1). These data indicate that the TM resistance is mediated by elevated HBP product availability due to reduced catabolism of GlcNAc-6P. To

further corroborate a causal role of AMDHD2 mutation in elevated UDP-GlcNAc levels and the accompanying TM resistance, we performed rescue experiments with N-terminally FLAG-HA-tagged human AMDHD2 (hAMDHD2). We compared the expression of WT hAMDHD2 and, based on information from the bacterial homolog N-acetylglucosamine-6-phosphate deacetylase (NagA)³², a potential catalytically inactive mutant with a D294A substitution (hAMDHD2 D294A) in control WT and AMDHD2 KO mESCs (Figure 2-figure supplement 2A, B). Overexpression of WT or mutant hAMDHD2 did not affect UDP-GlcNAc levels or TM resistance in WT mESCs (Figure 2C, D). However, in AMDHD2 KO cells only re-expression of functional WT hAMDHD2 reduced UDP-GlcNAc levels, while overexpression of the inactive hAMDHD2 D294A mutant still resulted in significantly elevated UDP-GlcNAc levels compared to WT cells. This observation was functionally supported by TM resistance assays using the same cell lines; overexpression of mutant hAMDHD2 D294A in the AMDHD2 KO background had no effect, but expression of WT hAMDHD2 reduced TM resistance. Together, these data emphasize the relevance of functional AMDHD2 for HBP activity and they show that AMDHD2 deletion results in TM resistance via increased HBP activity.

To better understand the physiological consequences of HBP activation through AMDHD2 regulation, we disrupted the *Amdhd2* locus to generate a KO mouse (Figure 2-figure supplement 2A-C). Although the *Amdhd2* mutation distributed in Mendelian ratios in the offspring, no viable homozygous *Amdhd2* KO pups were weaned (Figure 2E), indicating a recessive mutation. Heterozygous animals however, did not show any macroscopic changes, although further analysis is still missing and alterations on a behavioral, anatomical, histological or

molecular level cannot be excluded. Homozygous *Amdhd2* KO embryos showed early embryonic lethality, indicating an essential function of AMDHD2 during development. Taken together, we identified AMDHD2 as novel regulator of the HBP important in mESCs and for embryonic development.

Structural and biochemical characterization of human AMDHD2

Until now, no structure of eukaryotic AMDHD2 was available and functional properties of human AMDHD2 remain largely unexplored. Therefore, we performed a structural and a biochemical characterization of human AMDHD2. Initial apo AMDHD2 crystals diffracted poorly and no structure could be solved. Based on homology to bacterial NagA, human AMDHD2 is likely to bind a divalent cation in the active site, potentially stabilizing the protein and supporting co-crystallization. Consequently, we analyzed the stabilizing effect of several divalent cations. Addition of CoCl_2 , NiCl_2 , and ZnCl_2 to the SEC buffer increased the thermal stability of AMDHD2 by 3-4°C (Figure 3A). Moreover, we tested the influence of CoCl_2 , NiCl_2 , and ZnCl_2 on the deacetylase activity of AMDHD2. For that purpose, the metal co-factor of AMDHD2 was first removed by incubation with EDTA and then CoCl_2 , NiCl_2 , or ZnCl_2 were added back. Addition of MgCl_2 served as negative control, while an untreated AMDHD2 was used as positive control. Both CoCl_2 and ZnCl_2 restored and ZnCl_2 even increased AMDHD2 activity (Figure 3B). Thus, Co^{2+} or Zn^{2+} might be the metal co-factor in human AMDHD2. We next tested co-crystallization of AMDHD2 with ZnCl_2 or CoCl_2 . While no crystals formed in the presence of CoCl_2 , the co-crystallization with ZnCl_2 yielded needle clusters in several conditions. Optimized crystals diffracted to a resolution limit of 1.84 Å (AMDHD2 + Zn) or 1.90 Å (AMDHD2 + Zn + GlcN6P). The data collection and refinement statistics

are summarized in Table 1. Human AMDHD2 is organized in two domains, a deacetylase domain responsible for the conversion of GlcNAc-6P into GlcN6P and a second small domain with unknown function (DUF) (Figure 3C, Figure 3-figure supplement 1). Residues from both the N-terminus and the C-terminus contribute to the DUF domain. The structure of AMDHD2 was almost completely modeled into the electron density map except for some N-terminal (1-5) and C-terminal residues (407-409). In the asymmetric unit, AMDHD2 forms a dimer through direct interactions of the deacetylase domains with an interface of 1117 \AA^2 and this dimeric assembly was judged as biological relevant by the EPPIC server³³. Although the dimer is formed by a rather small interface, this conformation is supported by the crystallographic B-factors, which show low values at the interface, indicating a mutual stabilization (Figure 3-figure supplement 2) and by dynamic light scattering (DLS) measurements, confirming the presence of AMDHD2 dimers in solution (Figure 3-figure supplement 3). A comparison between both monomers from the dimer in the crystal revealed no major structural differences between monomer A and monomer B (Figure 3-figure supplement 4). The structure of the deacetylase domain showed a TIM (triosephosphate isomerase) barrel-like fold (Figure 3D). A typical TIM-barrel has eight alternating β -strands and α -helices forming a barrel shape where the parallel β -sheet builds the core that is surrounded by the α -helices. In AMDHD2, the eight alternating β -strands/ α -helices are interrupted after eight β -strands and seven α -helices by an insertion of three antiparallel β -strands (β 15- β 17), which form an additional β -sheet close to the active site (Figure 3C, Figure 3-figure supplement 5). In monomer B, this β -sheet shows the highest crystallographic B-factors within the structure

(Figure 3-figure supplement 2), indicating high flexibility and suggesting a functional role as a lid to the active site. The DUF-domain consists of two β -sheets, which are composed of three or six antiparallel β -strands each, and two small α -helices (Figure 3D). Together, these β -sheets form a β -sandwich. A superposition of the Zn-bound and the GlcN6P- and Zn-bound structures of AMDHD2 indicated no structural changes by the binding of the product (Figure 3-figure supplement 6). Residues from both monomers contribute to GlcN6P-binding (Figure 3E, Figure 3-figure supplement 7A). The phosphate group of the sugar is interacting via hydrogen bonds with Asn235 and Ala236, as well as ionic interactions to His242* and Arg243* of the other monomer (Figure 3E, Figure 3-figure supplement 7A,B). To assess a functional role of the residues His242* and Arg243*, and especially of the dimeric state on catalytic activity of AMDHD2, we generated the double mutant H242A/R243A and the mutants I280E and I280R, whose side chains might disrupt dimerization (Figure 3F). Analytical size-exclusion chromatography measurements confirmed the presence of monomeric I280E (45.7 ± 0.1 kDa) and monomeric I280R (44.4 ± 0.5 kDa) compared to dimeric wildtype AMDHD2 (89.2 ± 0.9 kDa) (Figure 3G,H). In contrast, the H242A/R243A substitution did not clearly disrupt dimerization (79.4 ± 0.8 kDa) (Figure 3G,H). Strikingly, I280E, I280R, and H242A/R243A showed no catalytic activity, supporting that AMDHD2 must form a dimer to be active and that the residues His242* and Arg243* are indispensable for catalytic activity. GlcN6P binding to the active site is further mediated by hydrogen bonds between the hydroxyl groups of GlcN6P with Ala154 and His272. The catalytic Zn ion is coordinated via electrostatic interactions with Glu143, His211, His232, and two water molecules, which in

turn are stabilized by interactions with GlcN6P and several amino acid side chains including Asp294 that might, based on the homology to bacterial NagA, act as the catalytic base³² (Figure 3E, Figure 3-figure supplement 7A,B). We confirmed the presence of a single Zn ion in the human AMDHD2 active site by measuring an anomalous signal at the Zn-K edge (Figure 3J). Given the conservation of all functional residues (Figure 3-figure supplement 8), the human AMDHD2 reaction mechanism is likely to be very similar to the proposed mechanism for the enzyme from *E. coli*³². In addition to GlcNAc-6P, bacterial NagAs are reported to use N-acetylgalactosamine-6-phosphate (GalNAc-6P) and N-acetylglucosamine-6-sulphate (GlcNAc-6S) as substrates, albeit with increased K_m values^{32,34}. The high structural conservation of the side chains interacting with the sugar's C4 for GalNAc-6P or the phosphate group prompted us to test whether human AMDHD2 can catalyze the deacetylation of GalNAc-6P and GlcNAc-6S as well. Of note, we did not observe activity towards these N-acetyl amino sugars that might be of physiological relevance (Figure 3-figure supplement 9). In summary, our data show that human AMDHD2 is an obligate dimeric protein with high specificity for GlcNAc-6P that carries a single catalytic Zn ion in the active center.

Characterization of AMDHD2 loss-of-function mutants

We next characterized the eleven AMDHD2 substitutions from our screen and the putative active site mutant D294A to understand how they might affect the function of AMDHD2. Many AMDHD2 variants were soluble upon bacterial expression, including F146L, A154P, T185A, S208T, and D294A (Figure 4A). These substitutions are located close to the active site of AMDHD2 (Figure 4B) and Ala154 is involved in ligand binding by donating an H-bond via its main

chain NH group to the 3-OH group of the sugar (Figure 3E, Figure 3-figure supplement 7A,B). In contrast, no soluble expression could be achieved for AMDHD2 G102D, G130R, G226E, and G265V (Figure 4A, Figure 4-figure supplement 1). The substitution of the small, flexible glycine by charged and/or bigger residues are likely to be incompatible with the proper tertiary structure and/or the folding process, thus resulting in insoluble AMDHD2 protein variants that remain in the pellet fraction after sample lysis (Figure 4-figure supplement 1). The effect of the L142F mutation was even more severe as the substitution of Leu142 by the bigger phenylalanine resulted in AMDHD2 fragmentation (Figure 4A). Also, the I38T and G265R substitutions reduced soluble expression, indicating disturbed protein folding. We next tested the consequences of the I38T, T185A, G265R, and D294A substitutions on AMDHD2 activity. AMDHD2 T185A showed reduced activity and no activity was detected for G265R and D294A, while the third substitution, I38T, remained active (Figure 4C). This result indicates a functional role of Asp294 in the catalytic mechanism, confirming our idea that this substitution inactivates AMDHD2 and justifying its use in the rescue experiments (Figure 2C,D). Asp294 is likely to act as catalytic base that activates the nucleophilic water molecule together with the metal ion, and later protonating the leaving group³². Moreover, the I38T substitution is the only identified mutation from the screen that is located in the DUF domain of AMDHD2. It reduced bacterial AMDHD2 expression yields, suggesting impaired protein folding. This is likely to result in a loss-of-function *in vivo*, while the purified and soluble protein is active. Taken together, the structural and biochemical characterization of AMDHD2 revealed

292 that loss-of-function and subsequent HBP activation resulted from folding
293 defects in AMDHD2 or it was caused by a loss of catalytic activity.

AMDHD2 limits HBP activity when GFPT2 replaces GFPT1 as the first enzyme

Having established that a loss of AMDHD2 function results in HBP activation, we wondered about the role of the HBP's rate limiting enzyme GFPT1. Under normal conditions, GFPT1 is constantly feedback inhibited by UDP-GlcNAc, crucially limiting HBP activity²⁵. A gain-of-function substitution in GFPT1 (G451E), however, increased HBP flux in nematodes and in murine cells, demonstrating a high degree of conservation²⁶. In AN3-12 cells, the G451E gain-of-function substitution, introduced into the genomic locus by CRISPR/Cas9, as well as a *Gfpt1* KO did not affect UDP-GlcNAc levels (Figure 5-figure supplement 1). While *Gfpt1* is widely expressed across cell types, it is known that in some tissues *Gfpt2* is the predominantly expressed paralog⁷. Since loss of GFPT1 did not affect HBP activity, we hypothesized that GFPT2 instead of GFPT1 might control metabolite entry into the HBP in AN3-12 mESCs. Indeed, *Gfpt2* mRNA was abundantly expressed in AN3-12 cells, while expression levels of *Gfpt1* were comparatively low (Figure 5A). Next, we performed WB analysis using pure purified human GFPT and compared those to the GFPT abundance in various cell lines. GFPT2 was found abundantly expressed, while GFPT1 was difficult to detect in AN3-12 mESCs (Figure 5B). E14 mESCs likewise showed predominant GFPT2 expression and low GFPT1 abundance. In contrast, mouse neuronal N2a cells as well as muscle precursor C2C12 myoblasts showed predominant GFPT1 expression and GFPT2 was virtually undetectable. These data suggest a HBP configuration characterized by a high GFPT2:GFPT1 ratio in mESCs.

To further investigate the possibility of ESC-specific HBP regulation, we next checked AMDHD2 levels in mESCs and compared them to cells using GFPT1 as the predominant first HBP enzyme. Mirroring GFPT2 levels, AMDHD2 protein abundance was higher in mESCs compared to N2a and C2C12 cells (Figure 5C). Moreover, the KO of AMDHD2 in AN3-12 mESCs resulted in a drastic elevation of UDP-GlcNAc levels, while the loss of AMDHD2 in N2a cells had no significant effect (Figure 5D). In accordance, the loss of AMDHD2 in C2C12 myoblasts was not sufficient to increase UDP-GlcNAc levels compared to control cells (Figure 5-figure supplement 2A-B). This indicates that AMDHD2 was constitutively active in AN3-12 cells, while the catalysis of the reverse flux of the HBP by AMDHD2 seemed to be negligible in N2a and C2C12 cells. We therefore hypothesized that AMDHD2 plays a key role in the HBP when GFPT2 is its first enzyme instead of the more common GFPT1. Our previous data indicate that GFPT1 is under constant UDP-GlcNAc inhibition, sufficient for full suppression of GFPT1 activity²⁵. We reasoned that higher UDP-GlcNAc levels in mESCs can only be achieved by differences in UDP-GlcNAc feedback inhibition between GFPT1 and GFPT2. To address this point, we generated recombinant human GFPT1 and GFPT2 with an internal His₆tag and characterized the proteins in activity assays (Figure 5E, Table 2, Figure 5-figure supplement 3A-B). Kinetic measurements confirmed that both proteins were fully functional and revealed different substrate affinities of GFPT2 compared to GFPT1 (Table 2, Figure 5-figure supplement 3A-B). In a UDP-GlcNAc dose response assay, we found a significantly higher IC₅₀ value for GFPT2 (367.3 - 43.6/+49,5 μM) compared to GFPT1 (57.0 -8.3/+9.7 μM) (Figure 5E, Table 2). We conclude, first, that UDP-GlcNAc inhibition is weaker in GFPT2 compared to

GFPT1 and, second, that AMDHD2 plays a crucial role in balancing GFPT2-mediated HBP flux. Consistent with lower feedback inhibition of GFPT2, UDP-GlcNAc levels in AN3-12 and E14 mESCs were significantly higher than in N2a and C2C12 cells with a GFPT1-regulated HBP (Figure 5F). We also tested protein O-GlcNAc modification, which relies on UDP-GlcNAc as a precursor molecule, in the different cell lines via Western blot analysis with an O-GlcNAc specific antibody (RL2). Consistent with the elevated UDP-GlcNAc levels, we observed significantly higher O-GlcNAc modification in mESCs. Of note, both OGA and OGT were more abundant in the mESCs compared to N2a and C2C12 cells (Figure 5G-J). Overall, these data demonstrate a mESC-specific configuration of the HBP, relying on the co-expression of GFPT2 and AMDHD2. This balance appears to be tuned to elevate UDP-GlcNAc levels and O-GlcNAc modification in ESCs.

Differentiation of ESCs induces an enzymatic reconfiguration of the HBP by reducing the GFPT2:GFPT1 ratio

In a next step, we asked if differentiation of mESC might affect the HBP's enzymatic configuration. For this, we removed leukemia inhibitory factor (LIF) from the medium, initiating differentiation³⁵. LIF removal for five days resulted in partial differentiation of AN3-12 cells as indicated by a decrease of stem cell markers (Figure 6-figure supplement 1A). Of note, GFPT2 protein as well as *Gfpt2* mRNA levels decreased significantly with LIF removal (Figure 6A,B). GFPT1 and AMDHD2 mRNA and protein levels did not change in this partial differentiation paradigm (Figure 6-figure supplement 1B-D). A decrease in the GFPT2:GFPT1 ratio upon differentiation was also observed in published datasets: relative GFPT2 mRNA and protein levels decrease during neuronal

368 differentiation³⁶ and during the differentiation in the cardiac lineage^{37,38} in
369 human ESCs (Figure 6C,D).

Discussion

HBP activation increases cellular UDP-GlcNAc levels that protect from TM toxicity³. We used this knowledge to interrogate the HBP for additional regulators in a forward genetic TM resistance screen using haploid mammalian cells. Random chemical DNA mutagenesis at high saturation in haploid cells is a unique strategy to identify recessive mutations including those leading to single amino acid substitutions. Using this approach, we identified the N-acetylglucosamine-6-phosphate deacetylase AMDHD2 as a novel regulator of the mammalian HBP. With an independent random insertional mutagenesis screen we confirmed the importance of AMDHD2 for regulating HBP activity and confirmed the role of AMDHD2 through rescue experiments. We next solved the first crystal structure of human AMDHD2 and noted that resistance-associated substitutions disturb protein folding or cluster in the catalytic pocket, likely interfering with substrate binding or catalysis. Finally, we found that mESCs utilize GFPT2 for metabolite entry into the HBP instead of the more widely expressed GFPT1. GFPT2 is under considerably reduced UDP-GlcNAc feedback inhibition explaining why loss of AMDHD2 activity was sufficient for HBP activation without GFPT mutations (Figure 6E).

Chemical mutagenesis-based screening in haploid cells represents a powerful and unique technique. This approach allows to dissect the entire spectrum of mutations including loss-of-function, gain-of-function, and neomorph alleles and at the same time allows structure-function analyses due to its amino acid resolution²⁸. The additional use of haploid cells not only enables detection of dominant but also recessive mutations due to the lack of a remaining and interfering WT allele. Of note, identification of AMDHD2 as a novel regulator of

the HBP was only possible in this specific setup since *Amdhd2* mutations are recessive as shown in the AMDHD2 KO mouse.

Besides the function as GlcNAc-6P deacetylase, AMDHD2 was shown to be involved in the degradation of N-glycolylneuraminic acid (Neu5Gc) in mice and in human cell culture^{11,39}. Nevertheless, mammalian AMDHD2 is rather unstudied and most knowledge is based on the bacterial homolog NagA. NagA catalyzes the deacetylation reaction in the HBP, contributing to recycling of cell wall components such as GlcNAc. Since breakdown of GlcNAc can be used as an energy source by bacteria and fungi, NagA plays a crucial role in their energy metabolism⁴⁰⁻⁴³. For this reason, HBP enzymes are attractive selective targets for antifungal and antibiotic drugs⁴⁴⁻⁴⁷. While catabolism of amino sugars connects GlcNAc with other important metabolic pathways, AMDHD2 had not been implicated in a regulatory role of the HBP and cellular UDP-GlcNAc homeostasis.

After identification of AMDHD2 as a key modulator of the mammalian HBP, we structurally and biochemically characterized human AMDHD2. We solved the structure of human AMDHD2, the first reported eukaryotic structure of an AMDHD2 homolog and confirmed that human AMDHD2 is an obligate dimeric enzyme. Residues from both monomers contribute to ligand binding in the active site, while the residues important for catalysis originate from one monomer. The oligomeric state of AMDHD2 is therefore a plausible target to modulate its catalytic properties.

We showed that the mutations identified in the screen cause a loss-of-function in human AMDHD2 by disrupting its folding or activity (Figure 4). AMDHD2 is composed of a deacetylase domain and a small domain with unknown function

(DUF). We identified only one mutation, I38T, within the DUF domain and this mutant showed diminished expression yields and low solubility, potentially explaining the loss-of-function. Nonetheless, the soluble fraction of AMDHD2 I38T was as active as wildtype AMDHD2 in activity assays, indicating that the DUF domain might be dispensable for catalysis.

Further characterizing the HBP, we noticed a surprising configuration of HBP enzymes in AN3-12 and E14 mESCs. While N2a cells and C2C12 myoblasts rely on GFPT1 as the key HBP enzyme, the mESCs use GFPT2 that is abundantly expressed (Figure 6E). Consistently, genetic manipulation of GFPT1 did not show any effect on UDP-GlcNAc levels in AN3-12 mESCs, while introducing the G451E gain-of-function mutation in GFPT1 of N2a cells leads to the previously reported boost of HBP activity²⁶. Additionally, AMDHD2 abundance was higher in mESCs (Figure 5C). In accordance, the AMDHD2 KO in AN3-12 mESCs massively elevated UDP-GlcNAc levels, while the loss of AMDHD2 in N2a cells and C2C12 myoblasts had no significant impact. Under physiological conditions, GFPT1 is strongly inhibited by UDP-GlcNAc²⁵. In this scenario, as is the case in N2a and C2C12 cells, loss of the reverse flux by AMDHD2 KO showed no drastic effect on UDP-GlcNAc levels (Figure 6E). Moreover, we showed that GFPT2 has altered substrate affinities and is less susceptible to UDP-GlcNAc feedback inhibition. N- or C-terminal tags in GFPT disturb the catalytic function, therefore the GFPT preparations used here carry an internal tag for purification at a position that is reported not to interfere with the kinetic properties of GFPT1⁴⁸. Studies with other tagging strategies reported only a weak inhibition of GFPT2 by UDP-GlcNAc^{49,50}. In contrast, we demonstrate that GFPT2 can be fully inhibited by UDP-GlcNAc with an

approximately 6-fold higher IC₅₀ value compared to GFPT1. Overall, our data suggest that GFPT1 is sufficiently regulated by feedback inhibition to determine HBP flux under physiological conditions. Cells using GFPT2 in the HBP, in contrast, rely on AMDHD2 to balance forward and reverse flux in the HBP. This HBP configuration might be a general adaptation of mESCs as we could show similar results for AN3-12 and E14 mESCs. Differentiation might result in a switch of GFPT expression and indeed partial differentiation of AN3-12 cells by LIF removal induced a significant decrease in GFPT2 levels. GFPT1 and AMDHD2 levels were not affected likely due to the early differentiation state. Analysis of published data confirmed that GFPT2 is highly expressed in human ESCs, and abundance decreased during neuronal or myocyte differentiation, indicating a conserved mechanism in human ESCs. Consistent with these findings, intestinal stem cells in *Drosophila melanogaster* likewise express GFPT2⁵¹. One potential consequence of this metabolic adaptation in ESCs is a higher baseline UDP-GlcNAc concentration compared to cells that use GFPT1 to control the HBP. This increase in UDP-GlcNAc concentration might affect downstream PTMs, which in turn can influence cell signaling. In particular, O-GlcNAc modifications already have been linked to stemness and pluripotency^{52,53}. Indeed, we detected increased O-GlcNAc levels in mESCs compared to cells utilizing GFPT1 in the HBP. Of note, not only UDP-GlcNAc levels but also the two essential enzymes for O-GlcNAc cycling OGA/OGT were significantly increased in mESCs, indicating a multilayered mechanism of maintaining high O-GlcNAc levels in mESCs. Additional significance of an ESC-specific HBP configuration might come from an adaptation to their special nutrient and energy requirements. ESCs show a specialized metabolic profile

that likely affect the concentrations of GFPT substrates⁵⁴. The kinetic properties of GFPT2 might reflect an adaption to substrate availability in ESCs. Consistently, GFPT2 is also upregulated in other rapidly proliferating cells with similar metabolic profiles, like in various types of cancer cells^{21,55-57}. Taken together, we identify AMDHD2 as a novel essential gene in embryonic development and describe a cell type-specific role of AMDHD2 acting in tandem with GFPT2 to regulate the HBP in ESCs. Tuning HBP metabolic activity is relevant in cellular stress resistance, oncogenic transformation, growth, and in age-related diseases as cancer, diabetes, cardiovascular diseases or neurodegenerative diseases^{1,21-23}. Of note, eukaryotic AMDHD2 was barely characterized and the identification of its critical role in HBP regulation paves the way for novel approaches to tackle age-associated pathologies, among other potential interventions. Our work advances the understanding of HBP control and provides specific means to beneficially affect these processes in the future.

Methods

Cell lines and culture conditions

AN3-12 mouse embryonic haploid stem cells were cultured as previously described²⁷. In brief, DMEM high glucose (Sigma-Aldrich) was supplemented with glutamine, fetal bovine serum (15%), penicillin/streptomycin, non-essential amino acids, sodium pyruvate (all Thermo Fisher Scientific, Waltham, Massachusetts), β -mercaptoethanol and LIF (both Merck Millipore) and used to culture cells at 37°C in 5% CO₂ on non-coated tissue culture plates. For partial differentiation of AN3-12 cells, cells were seeded at a density of 2000-3000 cells/6-well and incubated for 5 days in medium without LIF.

N2a mouse neuroblastoma cells (RRID:CVCL_0470) and C2C12 (RRID:CVCL_0188) cells were cultured in DMEM containing 4.5 g/l glucose (Gibco) supplemented with 10% fetal bovine serum (Gibco) and penicillin/streptomycin at 37°C in 5% CO₂. No mycoplasma contamination was detected.

Cell sorting

To maintain a haploid cell population cells were stained with 10 μ g/ml Hoechst 33342 (Thermo Fisher Scientific) for 30 min at 37°C. To exclude dead cells propidium iodide (Sigma-Aldrich) staining was added. Cells were sorted for DNA content on a FACSAria Fusion sorter and flow profiles were recorded with the FACSDiva software (BD Franklin Lakes).

Cell viability assay (XTT)

Relative cell viability was assessed using the XTT cell proliferation Kit II (Roche Diagnostics) according to the manufacturer's instructions. Tunicamycin

treatments were performed for 48 hours, starting 24 hours after cell seeding.
XTT turnover was normalized to corresponding untreated control cells.

ENU mutagenesis screen, exome sequencing, and analysis

The screening procedure and the data analysis were extensively described previously²⁸. In brief, AN3-12 mouse embryonic haploid stem cells were mutagenized with 0.01 mg/ml Ethylnitrosourea for 2h at room temperature prior to drug selection starting 24 hours post mutagenesis using 0.5 µg/ml tunicamycin (Merck-Milipore). After 21 days of drug selection, resistant clones were isolated and subjected to tunicamycin cytotoxicity assays and gDNA extraction using the Gentra Puregene Tissue Kit (Qiagen). Paired end, 150 bp whole exome sequencing was performed on an Illumina Novaseq 6000 instrument after precapture-barcoding and exome capture with the Agilent SureSelect Mouse All Exon kit. For data analysis, raw reads were aligned to the reference genome mm9. Variants were identified and annotated using GATK (v.3.4.46) and snpEff (v.4.2). Tunicamycin resistance causing alterations were identified by allelism only considering variants with moderate or high effect on protein and a read coverage > 10.

Retroviral-based insertional mutagenesis screen and integration site mapping

The generation of a comprehensive cell bank of haploid AN3-12 cells, containing insertions in 16.970 mouse genes, was already created and described elsewhere⁵⁸ (www.haplobank.at). In short, for retroviral library generation enhanced gene-trap (EGT) viruses carrying a neomycin-resistance cassette were packaged in PlatinumE (Cell Biolabs) cells. The virus was concentrated by centrifugation (25,000 r.p.m., 4°C, 4h) and haploid mESCs

were infected for 8 h in the presence of 2 µg/ml polybrene. Upon infection for 30h, cells were treated with 0.2 mg/ml G418 (Gibco) for selection of gene-trap insertions. To estimate numbers of integrations 500.000 cells were plated on 15 cm dishes, selected for integrations using G418 selection and colonies counted after 10 days. For comparison, 5.000 cells were plated without selection. From the barcoded AN3-12 Retro Library, 3 million cells were plated on 15 cm plates and drug selection was performed for 21 days starting 24h post mutagenesis using 0.5 µg/ml tunicamycin (Merck Millipore). Resistant clones were isolated and subjected to tunicamycin cytotoxicity assays. Mapping of the genomic integration site was performed by inverse PCR. The genomic region was amplified using the primers “DS” and “US” (primers are listed in Supplementary File 1). The PCR reaction was analyzed on an agarose gel, purified and used for Sanger Sequencing with primer “DS”. Sequences were analyzed manually with the USCS Genome Browser.

Generation of stable cell lines

For the generation of stable cell lines human AMDHD2 isoform 1 was integrated into the FLAG-HA-pcDNA3.1 plasmid (RRID:Addgene_52535) using XbaI and HindIII restriction sites. Cell lines stably overexpressing hAMDHD2 variants were generated by transfection of WT or AMDHD2 KO AN3-12 cells with FLAG-HA-hAMDHD2-pcDNA3.1 plasmids. For each variant, a 6 well was transfected with 4 µg of plasmid DNA with Lipofectamine 2000 (Life Technologies™) according to the manufacturer's protocol. The selection was performed with 0.4 mg/ml G418 (Gibco) for several weeks.

Gene editing and genotyping by Sanger sequencing

The specific GFPT1 G451E substitution as well as the KO of GFPT1 and AMDHD2 was engineered in AN3-12 cells (for the AMDHD2 KO also in N2a cells and C2C12 cells) using the CRISPR/Cas9 technology as described previously⁵⁹. DNA template sequences for small guide RNAs were designed online (<http://crispor.org>, Supplementary File 1), purchased from Sigma, and cloned into the Cas9-GFP expressing plasmid PX458 (RRID:Addgene_48138). Corresponding guide and Cas9 expressing plasmids were co-transfected with a single stranded DNA repair template (Integrated DNA technologies), using Lipofectamine 3000 (Thermo Fisher Scientific) according to manufacturer's instructions. For the AN3-12 cells three different AMDHD2 KO lines were generated, using different guide combinations (clone 1 = guide 1+2, clone 2 = guide 3+4, clone 3 = guide 1+5). GFP positive cells were singled using FACS Aria Fusion sorter and subjected to genotyping. DNA was extracted (DNA extraction solution, Epicentre Biotechnologies) and edited regions were specifically amplified by PCR (primers are listed in Supplementary File 1). Sanger sequencing was performed at Eurofins Genomics GmbH (Ebersberg, Germany).

RNA isolation and qPCR

Cells were collected in QIAzol (Qiagen) and snap frozen in liquid nitrogen. Samples were subjected to three freeze/thaw cycles (liquid nitrogen/ 37°C water bath) before addition of another half of the total QIAzol volume. After incubation for 5 min at RT, 200 µl chloroform were added per 1 ml QIAzol. Samples were vortexed, incubated for 2 min at RT, and centrifuged at 10.000 rpm and 4°C for 15 min. The aqueous phase was mixed with an equal volume of 70% ethanol

and transferred to a RNeasy Mini spin column (Qiagen). The total RNA was isolated using the RNeasy Mini Kit (Qiagen) and cDNA was subsequently generated by iScript cDNA Synthesis Kit (BioRad). qPCR was performed with Power SYBR Green master mix (Applied Biosystems) on a ViiA 7 Real-Time PCR System (Applied Biosystems). GAPDH expression functioned as internal control. All used primers for qPCR analysis are listed in Supplementary File 1.

Anion exchange chromatography mass spectrometry (IC-MS) analysis of UDP-GlcNAc and UDP-GalNAc

Cells were subjected to methanol:acetonitrile:mili-Q ultrapure water (40:40:20 [v:v:v]) extraction. UDP-GlcNAc and UDP-GalNAc (UDP-HexNAc) concentrations were measured using IC-MS analysis. Extracted metabolites were re-suspended in 500 µl of Optima LC/MS grade water (Thermo Fisher Scientific) of which 100 µl were transferred to polypropylene autosampler vials (Chromatography Accessories Trott, Germany). The samples were analyzed using a Dionex ionchromatography system (ICS5000, Thermo Fisher Scientific) connected to a triple quadrupole MS (Waters, TQ). In brief, 10 µl of the metabolite extract were injected in full loop mode using an overfill factor of 3, onto a Dionex IonPac AS11-HC column (2 mm × 250 mm, 4 µm particle size, Thermo Scientific) equipped with a Dionex IonPac AG11-HC guard column (2 mm × 50 mm, 4 µm, Thermo Scientific). The column temperature was held at 30°C, while the auto sampler was set to 6°C. The metabolite separation was carried using a KOH gradient at a flow rate of 380 µl/min, applying the following gradient conditions: 0-8 min, 30-35 mM KOH; 8-12 min, 35–100 mM KOH; 12-15 min, 100 mM KOH, 15-15.1 min, 10 mM KOH. The column was re-equilibrated at 10 mM for 4 min. UDP-HexNAcs were detected using multiple

reaction monitoring (MRM) mode with the following settings: capillary voltage 2.7 kV, desolvation temperature 550°C, desolvation gas flow 800 l/h, collision cell gas flow 0.15 ml/min. The transitions for UDP-GalNAc, as well as for UDP-GlcNAc were m/z 606 [M-H⁺]⁺ for the precursor mass and m/z 385 [M-H⁺]⁺ for the first and m/z 282 [M-H⁺]⁺ for the second transition mass. The cone voltage was set to 46V and the collision energy was set to 22V. UDP-GalNAc eluted at 10.48 min and UDP-GlcNAc eluted at 11.05 min. MS data analysis was performed using the TargetLynx Software (Version 4.1, Waters). Absolute compound concentrations were calculated from response curves of differently diluted authentic standards treated and extracted as the samples.

Immunoblot analysis

Protein concentration of cell lysates was determined using the PierceTM BCA protein assay kit according to manufacturer's instructions (ThermoFisher Scientific). Samples were adjusted in 5xLDS sample buffer containing 50 mM DTT. After boiling and a sonication step, equal protein amounts were subjected to SDS-PAGE and blotted on a nitrocellulose membrane using the Trans-Blot Turbo Transfer system (BioRad). All antibodies were used in 5% low-fat milk or 5% BSA in TBS-Tween. After incubation with HRP-conjugated secondary antibody, the blot was developed using ECL solution (Merck Millipore) on a ChemiDoc MP Imaging System (BioRad).

The following antibodies were used in this study: GFPT1 (RRID:AB_10975709, 1:1000), GFPT2 (RRID:AB_2868470, 1:5000), O-Linked N-Acetylglucosamine Antibody (ms, clone RL2, MABS157, Sigma-Aldrich, 1:1000), OGA (RRID:AB_10672079, 1:500), OGT (RRID:AB_2798857, 1:1000), FLAG (RRID:AB_262044, 1:2000), AMDHD2 (ms, S6 clone, in-house produced,

1:500), α -TUBULIN (RRID:AB_477593, 1:5000), rabbit IgG (RRID:AB_2536530, 1:5000), and mouse IgG (RRID:AB_2536527, 1:5000).

Generation of anti-AMDHD2 antibody

To generate monoclonal antibodies directed against AMDHD2, His-tagged human AMDHD2 was expressed in *Escherichia coli*, affinity purified, and used for immunization of eight-week-old male Balb/cJRj mice. The first immunization with 80 μ g of recombinant protein was enhanced by Freund's complete adjuvant; subsequent injections used 40 μ g protein with Freund's incomplete adjuvant. After multiple immunizations, the serum of the mice was tested for immunoreaction by enzyme-linked immunosorbent assay (ELISA) with the recombinant His-hAMDHD2 protein. In addition, the serum was used to stain immunoblots with lysates of HEK293T cells overexpressing FLAG-HA-hAMDHD2. After this positive testing, cells from the popliteal lymph node were fused with mouse myeloma SP2/0 cells by a standard fusion protocol. Monoclonal hybridoma lines were characterized, expanded, and subcloned according to standard procedures⁶⁰. Initial screening of clones was performed by ELISA with recombinant His-AMDHD2 protein and immunoblots using FLAG-HA-hAMDHD2 overexpressed in HEK293T cells. Isotyping of selected clones was performed with Pierce Rapid Isotyping Kit (Thermo Scientific, #26179). Final validation of antibody specificity was done by immunoblots of WT N2a cells compared to cells overexpressing FLAG-HA-hAMDHD2 and AMDHD2 KO cells.

Expression and purification of human AMDHD2

655 A pET28a(+)-AMDHD2 plasmid was purchased from BioCat (Heidelberg,
656 Germany), where human AMDHD2 isoform 1 was integrated in pET28a(+)
657 using NdeI and HindIII restriction sites. This vector was used to recombinantly
658 express human AMDHD2 isoform 1 with N-terminal His₆tag and a thrombin
659 cleavage site under the control of the T7 promoter in BL21 (DE3) *E. coli*. LB
660 cultures were incubated at 37°C and 180 rpm until an OD₆₀₀ of 0.4-0.6 was
661 reached. Then, protein expression was induced by addition of 0.5 mM
662 isopropyl-β-D-1-thiogalactopyranosid (IPTG) and incubated for 20-22 h at 20°C
663 and 180 rpm. Before harvest, a sample corresponding to an OD₆₀₀ of 0.5 was
664 taken, lysed in BugBuster® Master Mix (Merck Millipore) and the total lysate, the
665 supernatant after centrifugation of the total lysate, as well as the insoluble pellet,
666 which was reconstituted by 8 M urea, were analyzed by SDS-PAGE. The main
667 cultures were harvested and pellets stored at -80°C. The purification buffers
668 were modified from Bergfeld *et al.*¹¹. *E. coli* were lysed in 50 mM Tris/HCl
669 pH 7.5, 100 mM NaCl, 20 mM imidazole, 1 mM Tris(2-carboxyethyl)phosphin
670 (TCEP) with complete EDTA-free protease inhibitor cocktail (Roche) and
671 10 µg/ml DNaseI (Sigma) by sonication. The lysate was clarified by
672 centrifugation and the supernatant loaded on Ni-NTA Superflow affinity resin
673 (Qiagen). The resin was washed with wash buffer (50 mM Tris-HCl, 100 mM
674 NaCl, 50 mM imidazole, 1 mM TCEP; pH 7.5) and the protein was eluted with
675 wash buffer containing 250 mM imidazole. The His₆-tag was proteolytically
676 removed using 5 Units of thrombin (Sigma-Aldrich) per mg protein overnight at
677 4°C. AMDHD2 was further purified according to its size on a HiLoad™ 16/60
678 Superdex™ 200 prep grade preppacked column (GE Healthcare) using an

679 ÄKTAprime chromatography system at 4°C with a SEC buffer containing 50 mM
680 Tris-HCl, 100 mM NaCl, 1 mM TCEP, 5 % glycerol; pH 7.5.

Site-directed mutagenesis

The AMDHD2 mutations were introduced into the pET28a(+)-AMDHD2 plasmid by site-directed mutagenesis as described previously⁶¹ (Mutagenesis primers are listed in Supplementary File 1). This protocol was also used to integrate an internal His₆-tag between Ser300 and Asp301 in human GFPT2 in the plasmid FLAG-HA-hGFPT2-pcDNA3.1 (pcDNATM3.1⁽⁺⁾, ThermoFisher Scientific #V79020). This position is equivalent to the internal His₆-tag in human GFPT1, which does not interfere with GFPT kinetic properties⁴⁸. The GFPT2 gene with internal His₆-tag was subsequently subcloned into the pFL vector for the generation of baculoviruses using XbaI and HindIII entry sites.

Thermal shift assay

The thermal stability of AMDHD2 was analyzed by thermal shift (thermofluor) assays. For this purpose, the proteins were incubated with SYPRO orange dye (Sigma-Aldrich), which binds specifically to hydrophobic amino acids leading to an increased fluorescence at 610 nm when excited with a wavelength of 490 nm. The melting temperature is defined as the midpoint of temperature of the protein-unfolding transition⁶². This turning point of the melting curve was extracted from the derivative values of the RFU curve, where a turning point to the right is a minimum. The influence of several divalent cations on the thermal stability of AMDHD2 was tested. For this, the SEC buffer was supplemented with MgCl₂, CaCl₂, MnCl₂, CoCl₂, NiCl₂, CuSO₄, ZnCl₂, or CdCl₂ at a final concentration of 10 µM. The reaction mixtures were pipetted in white RT-PCR plates and contained 5 µl SYPRO orange dye (1:500 dilution in ddH₂O) and 5-10 µg protein in a total volume of 50 µl. The plates were closed with optically clear tape and placed in a BioRad CFX-96 Real-Time PCR machine. The

melting curves were measured at 1°C/min at the FRET channel in triplicate measurements and the data analyzed with CFX Manager™ (BioRad).

AMDHD2 activity assay

The deacetylase activity of AMDHD2 was determined by following the cleavage of the amide/peptide bond of the N-acetyl amino sugars GlcNAc6P, GalNAc6P, or GlcNAc6S at 205 nm in UV transparent 96 well microplates (F-bottom, Brand #781614). The assay mix contained 1 mM N-acetyl amino sugar in 50 mM Tris-HCl pH 7.5 and was pre-warmed for 10 min at 37 °C in the plate reader. The reaction was started by adding 20 pmol AMDHD2 and was monitored several minutes at 37°C. The initial reaction rates (0-1 min) were determined by Excel (Microsoft) and the amount of consumed GlcNAc6P was calculated from a GlcNAc6P standard curve. All measurements were performed in duplicates. For the analysis of the impact of several divalent metal ions on the activity of AMDHD2, the protein was incubated for 10 min with 0.1 µM EDTA and afterwards 10 µM divalent was added to potentially restore activity.

Human AMDHD2 crystallization and crystal soaking

Human AMDHD2 was co-crystallized with a 1.25x ratio (molar) of ZnCl₂ at a concentration of 9 mg/ml in sitting-drops by vapor diffusion at 20°C. Intergrown crystal plates formed in the PACT *premier*™ HT-96 (Molecular Dimensions) screen in condition H5 with a reservoir solution containing 0.1 M bis-tris propane pH 8.5, 0.2 M sodium nitrate, and 20% (w/v) PEG3350. In an optimization screen, the concentration of PEG3350 was constant at 20 % (w/v), while the pH value of bis-tris propane and the concentration of sodium nitrate were varied. The drops were set up in 1.5 µl protein solution to 1.5 µl precipitant solution and 2 µl protein solution to 1 µl precipitant solution. Best crystals were

obtained with a drop ratio of 2 μ l protein solution to 1 μ l precipitant solution at 0.1 M bis tris propane pH 8.25, 0.25 M sodium nitrate, and 20% (w/v) PEG3350. 5 mM GlcN6P in reservoir solution was soaked into the crystals for 2 to 24h. For crystal harvesting, the intergrown plates were separated with a needle and 15% glycerol was used as cryoprotectant.

Data collection and refinement

X-ray diffraction measurements were performed at beamline P13 at PETRA III, DESY, Hamburg (Germany) and beamline X06SA at the Swiss Light Source, Paul Scherrer Institute, Villigen (Switzerland). The diffraction images were processed by XDS⁶³. The structure of human AMDHD2 was determined by molecular replacement^{64,65} with phenix.phaser^{66,67} using the models of *B. subtilis* AMDHD2 (PDB 2VHL) as search model. The structures were further manually built using COOT⁶⁸ and iterative refinement rounds were performed using phenix.refine⁶⁷. The structure of GlcN6P soaked crystals was solved by molecular replacement using our human AMDHD2 structure as search model. Geometry restraints for GlcN6P was generated with phenix.elbow software⁶⁷. Structures were visualized using PyMOL (Schrödinger) and 2D ligand-protein interaction diagrams were generated using LigPlot+⁶⁹.

Analytical size-exclusion chromatography

The molecular weight of AMDHD2 and several mutants was determined by analytical size-exclusion chromatography on a Superdex™ 200 Increase 10/300 GL prepacked column (GE Healthcare) using an ÄKTApurifier chromatography system at 20°C. The measurement was performed with 100 μ l protein (5 mg/ml) in 50 mM Tris-HCl, 100 mM NaCl, 1 mM TCEP, 5 % glycerol; pH 7.5. All measurements were performed in triplicates and the molecular

weight was calculated from a standard curve from proteins with known molecular weights.

Dynamic Light Scattering (DLS)

DLS measurements were performed to analyze the size distribution of AMDHD2 in solution. Directly before measurement, 100 µl protein solution was centrifuged for 10 min at 15,000 g to remove any particles from solution and 70 µl of the supernatant was transferred into a UV disposable cuvette (UVette® 220-1600 nm, Eppendorf #952010051). The cuvette was placed in a Wyatt NanoStar DLS machine and the measurement performed with 10 frames with 10 sec/frame. Data were analyzed with the software Dynamics and converted to particle size distribution functions. The scattering intensity (%) was plotted against the particle radius (nm) in a histogram.

Baculovirus generation and insect cell expression of GFPT

Sf21 (RRID:CVCL_0518) suspension cultures were maintained in SFM4Insect™ HyClone™ medium with glutamine (GE Lifesciences) in shaker flasks at 27°C and 90 rpm in an orbital shaker. GFPT1 and GFPT2 were expressed in *Sf21* cells using the MultiBac baculovirus expression system⁷⁰. In brief, GFPT (from the pFL vector) was integrated into the baculovirus genome via Tn7 transposition and maintained as bacterial artificial chromosome in DH10EMBacY *E. coli* cells. Recombinant baculoviruses were generated by transfection of *Sf21* with bacmid DNA. The obtained baculoviruses were used to induce protein expression in *Sf21* cells.

GFPT1 and GFPT2 purification

Sf21 cells were lysed by sonication in lysis buffer (50 mM Tris/HCl pH 7.5, 200 mM NaCl, 10 mM Imidazole, 2 mM TCEP, 0.5 mM Na₂Frc6P, 10% (v/v) glycerol) supplemented with complete EDTA-free protease inhibitor cocktail (Roche) and 10 µg/ml DNaseI (Sigma-Aldrich). Cell debris and protein aggregates were removed by centrifugation and the supernatant was loaded on a Ni-NTA Superflow affinity resin (Qiagen). The resin was washed with lysis buffer and the protein eluted with lysis buffer containing 200 mM imidazole. The proteins were further purified according to their size on a HiLoad™ 16/60 Superdex™ 200 prep grade preppacked column (GE Healthcare) using an ÄKTAprime chromatography system at 4°C with a SEC buffer containing 50 mM Tris/HCl, pH 7.5, 2 mM TCEP, 0.5 mM Na₂Frc6P, and 10% (v/v) glycerol.

GDH-coupled activity assay and UDP-GlcNAc inhibition

GFPT's amidohydrolysis activity was measured with a coupled enzymatic assay using bovine glutamate dehydrogenase (GDH, Sigma-Aldrich G2626) in 96 well standard microplates (F-bottom, BRAND #781602) as previously described⁴⁸ with small modifications. In brief, the reaction mixtures contained 6 mM Frc6P, 1 mM APAD, 1 mM EDTA, 50 mM KCl, 100 mM potassium-phosphate buffer pH 7.5, 6.5 U GDH per 96 well and for L-Gln kinetics varying concentrations of L-Gln. For UDP-GlcNAc inhibition assays the L-Gln concentration was kept at 10 mM. The plate was pre-warmed at 37°C for 10 min and the activity after enzyme addition was monitored continuously at 363 nm in a microplate reader. The amount of formed APADH was calculated with $\epsilon_{(363 \text{ nm, APADH})} = 9100 \text{ l} \cdot \text{mol}^{-1} \cdot \text{cm}^{-1}$. Reaction rates were determined by Excel (Microsoft) and K_m ,

v_{\max} , and IC_{50} were obtained from Michaelis Menten or dose response curves, which were fitted by Prism 8 software (Graphpad).

GNA1 expression and purification

The expression plasmid for human GNA1 with N-terminal His₆-tag was cloned previously²⁵. Human GNA1 with N-terminal His₆-tag was expressed in Rosetta (DE3) *E. coli* cells. LB cultures were incubated at 37°C and 180 rpm until an OD₆₀₀ of 0.4-0.6 was reached. Then, protein expression was induced by addition of 0.5 mM IPTG and incubated for 3 h at 37°C and 180 rpm. Cultures were harvested and pellets stored at -80°C. Human GNA1 purification protocol was adopted from Hurtado-Guerrero et al.⁷¹ with small modifications. *E. coli* were lysed in 50 mM HEPES/NaOH pH 7.2, 500 mM NaCl, 10 mM imidazole, 2 mM 2-mercaptoethanol, 5% (v/v) glycerol with complete EDTA-free protease inhibitor cocktail (Roche) and 10 µg/ml DNaseI (Sigma-Aldrich) by sonication. The lysate was clarified by centrifugation and the supernatant loaded on Ni-NTA Superflow affinity resin (Qiagen). The resin was washed with wash buffer (50 mM HEPES/NaOH pH 7.2, 500 mM NaCl, 50 mM imidazole, 5% (v/v) glycerol) and the protein was eluted with wash buffer containing 250 mM imidazole. Eluted protein was then dialyzed against storage buffer (20 mM HEPES/NaOH pH 7.2, 500 mM NaCl, 5% (v/v) glycerol).

GNA1 and GNA1-coupled activity assays

The activity of human GNA1 was measured in 96 well standard microplates (F-bottom, BRAND #781602) as described previously⁷². For kinetic measurements, the assay mixture contained 0.5 mM Ac-CoA, 0.5 mM DTNB, 1 mM EDTA, 50 mM Tris/HCl pH 7.5 and varying concentrations of D-GlcN6P.

The plates were pre-warmed at 37°C and reactions were initiated by addition of GNA1. The absorbance at 412 nm was followed continuously at 37°C in a microplate reader. The amount of produced TNB, which matches CoA production, was calculated with $\epsilon_{(412 \text{ nm, TNB})} = 13800 \text{ l} \cdot \text{mol}^{-1} \cdot \text{cm}^{-1}$. Typically, GNA1 preparations showed a K_m of $0.2 \pm 0.1 \text{ mM}$ and a k_{cat} of $41 \pm 8 \text{ sec}^{-1}$. GFPT's D-GlcN6P production was measured in a GNA1-coupled activity assay following the consumption of AcCoA at 230 nm in UV transparent 96 well microplates (F-bottom, Brand #781614) as described by Li et al.⁷². In brief, the assay mixture contained 10 mM L-Gln, 0.1 mM AcCoA, 50 mM Tris/HCl pH 7.5, 2 µg hGNA1 and varying concentrations of Frc6P. The plates were incubated at 37°C for 4 min and reactions started by adding L-Gln. Activity was monitored continuously at 230 nm and 37°C in a microplate reader. The amount of consumed AcCoA was calculated with $\epsilon_{(230 \text{ nm, AcCoA})} = 6436 \text{ l} \cdot \text{mol}^{-1} \cdot \text{cm}^{-1}$. As UDP-GlcNAc absorbs light at 230 nm, the GNA-1-coupled assay cannot be used to analyze UDP-GlcNAc effects on activity.

CRISPR/Cas9-mediated generation of transgenic mice

CRISPR/Cas9-mediated generation of AMDHD2 KO mice was performed by ribonucleoprotein complex injection in mouse zygotes. Guide RNAs (crRNAs) targeting exon 4 of the *Amdhd2* locus were designed online (crispor.org) and purchased from IDT. crRNA and tracrRNA were resuspended in injection buffer (1 mM Tris-HCl pH 7.5, 0.1 mM EDTA) and annealed at 1:1 molar concentration in a thermocycler (95°C for 5 min, ramp down to 25°C at 5°C/min). To prepare the injection mix (100 µl), two guide RNAs and the Cas9 enzyme (*S. pyogenes*, NEB) were diluted to a final concentration of 20 ng/µl each in injection buffer. The mix was incubated for 10-15 min at room temperature to allow

ribonucleoprotein complex assembly. After centrifugation, 80 µl of the supernatant were passed through a filter (Millipore, UFC30VV25). Both centrifugation steps were performed for 5 min at 13.000 rpm at room temperature. The filtered injection mix was used for zygote injections.

Mouse Zygote Microinjections

3- to 4-week-old C57Bl/6J females were superovulated by intraperitoneal injection of Pregnant Mare Serum Gonadotropin (5 IU) followed by intraperitoneal injection of Human Chorionic Gonadotropin hormone (5 IU Intervet Germany) 48h later. Superovulated females were mated with 10 to 20 week old stud males. The mated females were euthanized the next day and zygotes were collected in M2 media (Sigma-Aldrich) supplemented with hyaluronidase (Sigma-Aldrich).

Fertilized oocytes were injected into the pronuclei or cytoplasm with the prepared CRISPR/Cas9 reagents. Injections were performed under an inverted microscope (Zeiss AxioObserver) associated micromanipulator (Eppendorf NK2) and the microinjection apparatus (Eppendorf Femtojet) with in-house pulled glass capillaries. Injected zygotes were incubated at 37°C, 5% CO₂ in KSOM (Merck) until transplantation. 25 zygotes were surgically transferred into one oviduct of pseudo-pregnant CD1 female mice.

All procedures have been performed in our specialized facility, followed all relevant animal welfare guidelines and regulations, and were approved by LANUV NRW 84-02.04.2015.A025.

Isolation of mouse genomic DNA from ear clips

Ear clips were taken by the Comparative Biology Facility at the Max Planck Institute for Biology of Ageing (Cologne, Germany) at weaning age (3-4 weeks

of age) and stored at -20°C until use. 150 µl ddH₂O and 150 µl directPCR Tail Lysis reagent (PeqLab) were mixed with 3 µl proteinase K (20 mg/ml in 25 mM Tris-HCl, 5 mM Ca₂Cl, pH 8.0, Sigma-Aldrich). This mixture was applied to the ear clips, which were then incubated at 56°C overnight (maximum 16 h) shaking at 300 rpm. Proteinase K was inactivated at 85°C for 45 min without shaking. The lysis reaction (2 µl) was used for genotyping PCR without further processing. For genotyping of mouse genomic DNA DreamTaq DNA polymerase (ThermoFisher Scientific) was used.

Alignments

Following UniProt IDs were used for the protein sequence alignment of AMDHD2: *Homo sapiens* isoform 1: Q9Y303-1, *Mus musculus*: Q8JZV7, *Caenorhabditis elegans*: P34480, *Candida albicans*: Q9C0N5, *Escherichia coli*: P0AF18, *Bacillus subtilis*: O34450. ClustalOmega (<https://www.ebi.ac.uk/Tools/msa/clustalo/>) was used to generate a multiple sequence alignment⁷³. The alignment was formatted with the ESPript3 server (esprict.ibcp.fr/)⁷⁴ and further modified.

Statistical analysis

Data are presented as mean ± SEM/SD or as mean + SEM/SD. The mean of technical replicates is plotted for each biological replicate. Biological replicates represent different passages of the cells that were seeded on independent days. Statistical significance was calculated using GraphPad Prism (GraphPad Software, San Diego, California). The statistical test used is indicated in the respective figure legend. Significance levels are * p<0.05, ** p<0.01, *** p<0.001 versus the respective control.

900 **Data availability**

901 Structural data reported in this study have been deposited in the Protein Data
902 Bank with the accession codes 7NUT [<https://doi.org/10.2210/pdb7NUT/pdb>]
903 and 7NUU [<https://doi.org/10.2210/pdb7NUU/pdb>].

904

References

- 1 Marshall, S., Bacote, V. & Traxinger, R. R. Discovery of a metabolic pathway mediating glucose-induced desensitization of the glucose transport system. Role of hexosamine biosynthesis in the induction of insulin resistance. *J Biol Chem* **266**, 4706-4712 (1991).
- 2 Ghosh, S., Blumenthal, H. J., Davidson, E. & Roseman, S. Glucosamine metabolism. V. Enzymatic synthesis of glucosamine 6-phosphate. *J Biol Chem* **235**, 1265-1273 (1960).
- 3 Denzel, M. S. *et al.* Hexosamine pathway metabolites enhance protein quality control and prolong life. *Cell* **156**, 1167-1178, doi:10.1016/j.cell.2014.01.061 (2014).
- 4 Wellen, K. E. *et al.* The hexosamine biosynthetic pathway couples growth factor-induced glutamine uptake to glucose metabolism. *Genes Dev* **24**, 2784-2799, doi:10.1101/gad.1985910 (2010).
- 5 Yamashita, K., Tachibana, Y., Ohkura, T. & Kobata, A. Enzymatic basis for the structural changes of asparagine-linked sugar chains of membrane glycoproteins of baby hamster kidney cells induced by polyoma transformation. *J Biol Chem* **260**, 3963-3969 (1985).
- 6 McClain, D. A. & Crook, E. D. Hexosamines and insulin resistance. *Diabetes* **45**, 1003-1009, doi:10.2337/diab.45.8.1003 (1996).
- 7 Oki, T., Yamazaki, K., Kuromitsu, J., Okada, M. & Tanaka, I. cDNA cloning and mapping of a novel subtype of glutamine:fructose-6-phosphate amidotransferase (GFAT2) in human and mouse. *Genomics* **57**, 227-234, doi:10.1006/geno.1999.5785 (1999).
- 8 Arreola, R., Valderrama, B., Morante, M. L. & Horjales, E. Two mammalian glucosamine-6-phosphate deaminases: a structural and genetic study. *FEBS Lett* **551**, 63-70, doi:10.1016/s0014-5793(03)00896-2 (2003).
- 9 Wang, J., Liu, X., Liang, Y. H., Li, L. F. & Su, X. D. Acceptor substrate binding revealed by crystal structure of human glucosamine-6-phosphate N-acetyltransferase 1. *FEBS Lett* **582**, 2973-2978, doi:10.1016/j.febslet.2008.07.040 (2008).
- 10 Weidanz, J. A. *et al.* N-acetylglucosamine kinase and N-acetylglucosamine 6-phosphate deacetylase in normal human erythrocytes and *Plasmodium falciparum*. *British journal of haematology* **95**, 645-653 (1996).
- 11 Bergfeld, A. K., Pearce, O. M., Diaz, S. L., Pham, T. & Varki, A. Metabolism of vertebrate amino sugars with N-glycolyl groups: elucidating the intracellular fate of the non-human sialic acid N-glycolylneuraminic acid. *J Biol Chem* **287**, 28865-28881, doi:10.1074/jbc.M112.363549 (2012).
- 12 Ricciardiello, F. *et al.* Inhibition of the Hexosamine Biosynthetic Pathway by targeting PGM3 causes breast cancer growth arrest and apoptosis. *Cell Death Dis* **9**, 377, doi:10.1038/s41419-018-0405-4 (2018).
- 13 Mio, T., Yabe, T., Arisawa, M. & Yamada-Okabe, H. The eukaryotic UDP-N-acetylglucosamine pyrophosphorylases. Gene cloning, protein expression, and catalytic mechanism. *J Biol Chem* **273**, 14392-14397, doi:10.1074/jbc.273.23.14392 (1998).
- 14 Thoden, J. B., Wohlers, T. M., Fridovich-Keil, J. L. & Holden, H. M. Human UDP-galactose 4-epimerase. Accommodation of UDP-N-acetylglucosamine within the active site. *J Biol Chem* **276**, 15131-15136, doi:10.1074/jbc.M100220200 (2001).

954 15 Hanisch, F. G. O-glycosylation of the mucin type. *Biol Chem* **382**, 143-149,
955 doi:10.1515/bc.2001.022 (2001).

956 16 Parodi, A. J. Role of N-oligosaccharide endoplasmic reticulum processing
957 reactions in glycoprotein folding and degradation. *The Biochemical journal*
958 **348 Pt 1**, 1-13 (2000).

959 17 Martinez-Seara Monne, H., Danne, R., Róg, T., Ilpo, V. & Gurtovenko, A.
960 Structure of Glycocalyx. *Biophysical Journal* **104**, 251a,
961 doi:<https://doi.org/10.1016/j.bpj.2012.11.1412> (2013).

962 18 Hart, G. W. Dynamic O-linked glycosylation of nuclear and cytoskeletal
963 proteins. *Annu Rev Biochem* **66**, 315-335,
964 doi:10.1146/annurev.biochem.66.1.315 (1997).

965 19 Haltiwanger, R. S., Blomberg, M. A. & Hart, G. W. Glycosylation of nuclear
966 and cytoplasmic proteins. Purification and characterization of a uridine
967 diphospho-N-acetylglucosamine:polypeptide beta-N-
968 acetylglucosaminyltransferase. *Journal of Biological Chemistry* **267**, 9005-
969 9013, doi:[https://doi.org/10.1016/S0021-9258\(19\)50380-5](https://doi.org/10.1016/S0021-9258(19)50380-5) (1992).

970 20 Dong, D. L. & Hart, G. W. Purification and characterization of an O-GlcNAc
971 selective N-acetyl-beta-D-glucosaminidase from rat spleen cytosol. *J Biol*
972 *Chem* **269**, 19321-19330 (1994).

973 21 Oikari, S. *et al.* UDP-sugar accumulation drives hyaluronan synthesis in
974 breast cancer. *Matrix Biology* **67**, 63-74 (2018).

975 22 Arnold, C. S. *et al.* The microtubule-associated protein tau is extensively
976 modified with O-linked N-acetylglucosamine. *J Biol Chem* **271**, 28741-
977 28744, doi:10.1074/jbc.271.46.28741 (1996).

978 23 Champattanachai, V., Marchase, R. B. & Chatham, J. C. Glucosamine protects
979 neonatal cardiomyocytes from ischemia-reperfusion injury via increased
980 protein-associated O-GlcNAc. *American Journal of Physiology-Cell Physiology*
981 **292**, C178-C187 (2007).

982 24 Heifetz, A., Keenan, R. W. & Elbein, A. D. Mechanism of action of tunicamycin
983 on the UDP-GlcNAc:dolichyl-phosphate Glc-NAc-1-phosphate transferase.
984 *Biochemistry* **18**, 2186-2192, doi:10.1021/bi00578a008 (1979).

985 25 Ruegenberg, S. *et al.* Loss of GFAT-1 feedback regulation activates the
986 hexosamine pathway that modulates protein homeostasis. *Nat Commun* **11**,
987 687, doi:10.1038/s41467-020-14524-5 (2020).

988 26 Horn, M. *et al.* Hexosamine Pathway Activation Improves Protein
989 Homeostasis through the Integrated Stress Response. *iScience* **23**, 100887,
990 doi:10.1016/j.isci.2020.100887 (2020).

991 27 Elling, U. *et al.* Forward and reverse genetics through derivation of haploid
992 mouse embryonic stem cells. *Cell Stem Cell* **9**, 563-574,
993 doi:10.1016/j.stem.2011.10.012 (2011).

994 28 Horn, M. *et al.* Unbiased compound-protein interface mapping and prediction
995 of chemoresistance loci through forward genetics in haploid stem cells.
996 (2018).

997 29 Allmeroth, K. *et al.* Bortezomib resistance mutations in PSMB5 determine
998 response to second-generation proteasome inhibitors in multiple myeloma.
999 *Leukemia*, doi:10.1038/s41375-020-0989-4 (2020).

1000 30 Elling, U. *et al.* A reversible haploid mouse embryonic stem cell biobank
1001 resource for functional genomics. *Nature* **550**, 114-118,
1002 doi:10.1038/nature24027 (2017).

1003 31 White, R. J. & Pasternak, C. A. The purification and properties of N-
1004 acetylglucosamine 6-phosphate deacetylase from *Escherichia coli*. *The*
1005 *Biochemical journal* **105**, 121-125, doi:10.1042/bj1050121 (1967).

1006 32 Hall, R. S., Xiang, D. F., Xu, C. & Raushel, F. M. N-Acetyl-D-glucosamine-6-
1007 phosphate deacetylase: substrate activation via a single divalent metal ion.
1008 *Biochemistry* **46**, 7942-7952, doi:10.1021/bi700543x (2007).

1009 33 Bliven, S., Lafita, A., Parker, A., Capitani, G. & Duarte, J. M. Automated
1010 evaluation of quaternary structures from protein crystals. *PLOS*
1011 *Computational Biology* **14**, e1006104, doi:10.1371/journal.pcbi.1006104
1012 (2018).

1013 34 Ahangar, M. S. *et al.* Structural and functional determination of homologs of
1014 the *Mycobacterium tuberculosis* N-acetylglucosamine-6-phosphate
1015 deacetylase (NagA). *J Biol Chem* **293**, 9770-9783,
1016 doi:10.1074/jbc.RA118.002597 (2018).

1017 35 Hocke, G. M., Cui, M. Z. & Fey, G. H. The LIF response element of the alpha 2
1018 macroglobulin gene confers LIF-induced transcriptional activation in
1019 embryonal stem cells. *Cytokine* **7**, 491-502, doi:10.1006/cyto.1995.0067
1020 (1995).

1021 36 Saez, I., Koyuncu, S., Gutierrez-Garcia, R., Dieterich, C. & Vilchez, D. Insights
1022 into the ubiquitin-proteasome system of human embryonic stem cells.
1023 *Scientific reports* **8**, 4092, doi:10.1038/s41598-018-22384-9 (2018).

1024 37 Frank, S. *et al.* yylncT Defines a Class of Divergently Transcribed lncRNAs
1025 and Safeguards the T-mediated Mesodermal Commitment of Human PSCs.
1026 *Cell Stem Cell* **24**, 318-327.e318, doi:10.1016/j.stem.2018.11.005 (2019).

1027 38 Bartsch, D. *et al.* Translational specialization in pluripotency by RBPMS
1028 poises future lineage-decisions. *bioRxiv*, 2021.2004.2012.439420,
1029 doi:10.1101/2021.04.12.439420 (2021).

1030 39 Campbell, P., Laurent, T. C. & Roden, L. Assay and properties of N-
1031 acetylglucosamine-6-phosphate deacetylase from rat liver. *Analytical*
1032 *biochemistry* **166**, 134-141 (1987).

1033 40 Liu, Y. *et al.* Pathway engineering of *Bacillus subtilis* for microbial
1034 production of N-acetylglucosamine. *Metab Eng* **19**, 107-115,
1035 doi:10.1016/j.ymben.2013.07.002 (2013).

1036 41 Plumbridge, J. An alternative route for recycling of N-acetylglucosamine
1037 from peptidoglycan involves the N-acetylglucosamine phosphotransferase
1038 system in *Escherichia coli*. *J Bacteriol* **191**, 5641-5647,
1039 doi:10.1128/JB.00448-09 (2009).

1040 42 Popowska, M., Osinska, M. & Rzczkowska, M. N-acetylglucosamine-6-
1041 phosphate deacetylase (NagA) of *Listeria monocytogenes* EGD, an essential
1042 enzyme for the metabolism and recycling of amino sugars. *Arch Microbiol*
1043 **194**, 255-268, doi:10.1007/s00203-011-0752-3 (2012).

1044 43 Yadav, V. *et al.* N-acetylglucosamine 6-phosphate deacetylase (nagA) is
1045 required for N-acetyl glucosamine assimilation in *Gluconacetobacter*
1046 *xylinus*. *PLoS One* **6**, e18099, doi:10.1371/journal.pone.0018099 (2011).

1047 44 Zhang, Y. *et al.* Genetic and structural validation of phosphomannomutase
1048 as a cell wall target in *Aspergillus fumigatus*. *Mol Microbiol*,
1049 doi:10.1111/mmi.14706 (2021).

1050 45 Swiatek, M. A., Tenconi, E., Rigali, S. & van Wezel, G. P. Functional analysis of
1051 the N-acetylglucosamine metabolic genes of *Streptomyces coelicolor* and

1052 role in control of development and antibiotic production. *J Bacteriol* **194**,
1053 1136-1144, doi:10.1128/JB.06370-11 (2012).

1054 46 Świątek, M. A., Urem, M., Tenconi, E., Rigali, S. & van Wezel, G. P. Engineering
1055 of N-acetylglucosamine metabolism for improved antibiotic production in
1056 *Streptomyces coelicolor* A3(2) and an unsuspected role of NagA in
1057 glucosamine metabolism. *Bioengineered* **3**, 280-285,
1058 doi:10.4161/bioe.21371 (2012).

1059 47 Lockhart, D. E. A. *et al.* Targeting a critical step in fungal hexosamine
1060 biosynthesis. *J Biol Chem* **295**, 8678-8691, doi:10.1074/jbc.RA120.012985
1061 (2020).

1062 48 Richez, C. *et al.* Expression and purification of active human internal His(6)-
1063 tagged L-glutamine: D-Fructose-6P amidotransferase I. *Protein Expr Purif*
1064 **54**, 45-53, doi:10.1016/j.pep.2007.01.015 (2007).

1065 49 Hu, Y., Riesland, L., Paterson, A. J. & Kudlow, J. E. Phosphorylation of mouse
1066 glutamine-fructose-6-phosphate amidotransferase 2 (GFAT2) by cAMP-
1067 dependent protein kinase increases the enzyme activity. *J Biol Chem* **279**,
1068 29988-29993, doi:10.1074/jbc.M401547200 (2004).

1069 50 Oliveira, I. A. *et al.* Enzymatic and structural properties of human
1070 glutamine:fructose-6-phosphate amidotransferase 2 (hGFAT2). *J Biol Chem*,
1071 doi:10.1074/jbc.RA120.015189 (2020).

1072 51 Mattila, J., Kokki, K., Hietakangas, V. & Boutros, M. Stem Cell Intrinsic
1073 Hexosamine Metabolism Regulates Intestinal Adaptation to Nutrient
1074 Content. *Developmental cell* **47**, 112-121.e113,
1075 doi:10.1016/j.devcel.2018.08.011 (2018).

1076 52 Constable, S., Lim, J. M., Vaidyanathan, K. & Wells, L. O-GlcNAc transferase
1077 regulates transcriptional activity of human Oct4. *Glycobiology* **27**, 927-937,
1078 doi:10.1093/glycob/cwx055 (2017).

1079 53 Jang, H. *et al.* O-GlcNAc regulates pluripotency and reprogramming by
1080 directly acting on core components of the pluripotency network. *Cell Stem*
1081 *Cell* **11**, 62-74, doi:10.1016/j.stem.2012.03.001 (2012).

1082 54 Intlekofer, A. M. & Finley, L. W. S. Metabolic signatures of cancer cells and
1083 stem cells. *Nature Metabolism* **1**, 177-188, doi:10.1038/s42255-019-0032-0
1084 (2019).

1085 55 Shaul, Y. D. *et al.* Dihydropyrimidine accumulation is required for the
1086 epithelial-mesenchymal transition. *Cell* **158**, 1094-1109 (2014).

1087 56 Zhang, W. *et al.* GFPT2-Expressing Cancer-Associated Fibroblasts Mediate
1088 Metabolic Reprogramming in Human Lung Adenocarcinoma. *Cancer Res* **78**,
1089 3445-3457, doi:10.1158/0008-5472.Can-17-2928 (2018).

1090 57 Szymura, S. J. *et al.* NF-κB upregulates glutamine-fructose-6-phosphate
1091 transaminase 2 to promote migration in non-small cell lung cancer. *Cell*
1092 *Communication and Signaling* **17**, 24, doi:10.1186/s12964-019-0335-5
1093 (2019).

1094 58 Elling, U. *et al.* Derivation and maintenance of mouse haploid embryonic
1095 stem cells. *Nature protocols*, doi:10.1038/s41596-019-0169-z (2019).

1096 59 Ran, F. A. *et al.* Genome engineering using the CRISPR-Cas9 system. *Nature*
1097 *protocols* **8**, 2281-2308, doi:10.1038/nprot.2013.143 (2013).

1098 60 Köhler, G. & Milstein, C. Continuous cultures of fused cells secreting
1099 antibody of predefined specificity. *Nature* **256**, 495-497,
1100 doi:10.1038/256495a0 (1975).

- 61 Zheng, L., Baumann, U. & Reymond, J. L. An efficient one-step site-directed and site-saturation mutagenesis protocol. *Nucleic Acids Res* **32**, e115, doi:10.1093/nar/gnh110 (2004).
- 62 Ericsson, U. B., Hallberg, B. M., Detitta, G. T., Dekker, N. & Nordlund, P. Thermofluor-based high-throughput stability optimization of proteins for structural studies. *Anal Biochem* **357**, 289-298, doi:10.1016/j.ab.2006.07.027 (2006).
- 63 Kabsch, W. Xds. *Acta Crystallogr D Biol Crystallogr* **66**, 125-132, doi:10.1107/S0907444909047337 (2010).
- 64 Hoppe, W. Die Faltmolekülmethode: Eine neue Methode zur Bestimmung der Kristallstruktur bei ganz oder teilweise bekannten Molekülstrukturen. *Acta Crystallogr A* **10**, 750-751 (1957).
- 65 Huber, R. Die automatisierte Faltmolekülmethode. *Acta Crystallogr A* **19**, 353-356 (1965).
- 66 McCoy, A. J. Solving structures of protein complexes by molecular replacement with Phaser. *Acta Crystallogr D Biol Crystallogr* **63**, 32-41, doi:10.1107/S0907444906045975 (2007).
- 67 Adams, P. D. *et al.* PHENIX: a comprehensive Python-based system for macromolecular structure solution. *Acta Crystallogr D Biol Crystallogr* **66**, 213-221, doi:10.1107/S0907444909052925 (2010).
- 68 Emsley, P., Lohkamp, B., Scott, W. G. & Cowtan, K. Features and development of Coot. *Acta Crystallogr D Biol Crystallogr* **66**, 486-501, doi:10.1107/S0907444910007493 (2010).
- 69 Laskowski, R. A. & Swindells, M. B. LigPlot+: multiple ligand-protein interaction diagrams for drug discovery. *J Chem Inf Model* **51**, 2778-2786, doi:10.1021/ci200227u (2011).
- 70 Berger, I., Fitzgerald, D. J. & Richmond, T. J. Baculovirus expression system for heterologous multiprotein complexes. *Nat Biotechnol* **22**, 1583-1587, doi:10.1038/nbt1036 (2004).
- 71 Hurtado-Guerrero, R. *et al.* Structural and kinetic differences between human and *Aspergillus fumigatus* D-glucosamine-6-phosphate N-acetyltransferase. *Biochem J* **415**, 217-223, doi:10.1042/BJ20081000 (2008).
- 72 Li, Y. *et al.* An enzyme-coupled assay for amidotransferase activity of glucosamine-6-phosphate synthase. *Anal Biochem* **370**, 142-146, doi:10.1016/j.ab.2007.07.031 (2007).
- 73 Sievers, F. *et al.* Fast, scalable generation of high-quality protein multiple sequence alignments using Clustal Omega. *Mol Syst Biol* **7**, 539, doi:10.1038/msb.2011.75 (2011).
- 74 Robert, X. & Gouet, P. Deciphering key features in protein structures with the new ENDscript server. *Nucleic Acids Res* **42**, W320-324, doi:10.1093/nar/gku316 (2014).

Acknowledgments

We thank all M.S.D. and U.B. laboratory members as well as L. Kurian, H. Bazzi, and D. Vilchez for helpful discussions. The FLAG-HA-hGFPT-2-pcDNA3.1 plasmid was kindly provided by C. Geisen (Max Planck Institute for Biology of Ageing, MPI-AGE). We thank Y. Hinze, S. Perin, and P. Giavalisco from the MPI-AGE metabolomics core facility. We thank K. Folz-Donahue, L. Schumacher, A. Just, and C. Kukat from the MPI-AGE FACS and imaging core facility. We thank F. Metge, and J. Boucas from the MPI-AGE bioinformatics core facility. We thank I. Vogt from the MPI-AGE transgenesis core facility. We thank the MPI-AGE comparative biology facility. We thank M. Grzonka for support with the E14 mESCs. We are grateful to S. Birkmann for support in the insect cell maintenance. We thank I. Grimm and S. Schäfer for their help with the AMDHD2 production and D. Feind for the site-directed mutagenesis of monomeric AMDHD2 mutants. Crystals were grown in the Cologne Crystallization facility (C₂f). We thank the staff of beamline X06SA at the Swiss Light Source, Paul Scherrer Institute, Villigen (Switzerland) and beamline P13 at PETRA III, DESY, Hamburg (Germany) for their support during data collection. This work was supported by the German Federal Ministry of Education and Research (BMBF, grant 01GQ1423A EndoProtect), by the German Research Foundation (DFG, Projektnummer 73111208-SFB 829, B11 and B14), by the European Commission (ERC-2014-StG-640254-MetAGEn), and by the Max Planck Society. The Cologne Crystallization Facility C₂f was supported by DFG grant INST 216/949-1 FUGG.

Competing interests

The authors declare no competing interest.

Figure legends

Figure 1: Chemical mutagenesis screen for tunicamycin resistance in haploid mESCs identifies AMDHD2

(A) Schematic representation of experimental workflow for TM resistance screen using ENU mutagenesis in combination with whole exome sequencing. (B) Schematic representation of the mouse *Amdhd2* locus. Amino acid substitutions identified in the screen are highlighted. (C) Cell viability (XTT assay) of four TM resistant clones (clone 1-4) identified via insertional mutagenesis compared to control WT AN3-12 mESCs. Cells were treated with 0.5 µg/ml TM for 48h (mean ± SEM, n=4, * p<0.05, ** p<0.01, One-way ANOVA Dunnett post-test). (D) Western blot analysis of CRISPR/Cas9 generated AMDHD2 KO AN3-12 mESCs compared to wildtype cells (WT). (E) Cell viability (XTT assay) of WT and AMDHD2 KO AN3-12 cells treated with 0.5 µg/ml TM for 48h (mean ± SEM, n=4, ** p<0.01, unpaired t-test). (F) Representative images of WT and AMDHD2 KO AN3-12 cells treated with 0.5 µg/ml TM for 48h or respective control. Scale bar, 275 µm. Figure supplements are available in Figure 1-figure supplement 1. Source data for this figure are available in Figure 1-source data 1-6.

Figure 2: Disruption of AMDHD2 mediates tunicamycin resistance via elevated HBP flux

(A) Schematic overview of the hexosamine pathway (blue box). The intermediate Frc6P from glycolysis is converted to UDP-GlcNAc, which is a precursor for glycosylation reactions. The enzymes are glutamine fructose-6-phosphate amidotransferase (GFPT1/2), glucosamine-6-phosphate N-acetyltransferase (GNA1), phosphoglucomutase (PGM3), UDP-N-acetylglucosamine pyrophosphorylase (UAP1), glucosamine-6-phosphate deaminase (GNPDA1/2), N-acetylglucosamine deacetylase (AMDHD2), UDP-GlcNAc:dolichylphosphate GlcNAc-1-phosphotransferase (GPT), and UDP-galactose-4'-epimerase (GALE). Red line indicates negative feedback inhibition of GFPT by UDP-GlcNAc. UDP-HexNAc is a precursor for various glycosylation reactions including N-glycosylation, O-glycosylation, and O-GlcNAcylation or the synthesis of proteoglycans and other glycoconjugates. N-glycosylation is inhibited by tunicamycin (TM). (B) IC-MS analysis of UDP-HexNAc levels of four TM resistant clones (clone 1-4) generated in insertional mutagenesis screen compared to control WT and AMDHD2 KO AN3-12 mESCs (mean ± SEM, n=5, ** p<0.01, *** p<0.001, One-way ANOVA Dunnett post-test). (C) IC-MS analysis of UDP-GlcNAc levels in WT and AMDHD2 KO AN3-12 cells expressing WT FLAG-HA-hAMDHD2 (hAMDHD2) and mutant FLAG-HA-hAMDHD2 D294A (hAMDHD2 D294A) (mean ± SEM, n=7, * p<0.05, ** p<0.01, ns = not significant, One-way ANOVA Tukey post-test). (D) Cell viability (XTT assay) of

WT and AMDHD2 KO AN3-12 mESCs expressing WT FLAG-HA-hAMDHD2 (hAMDHD2) and mutant FLAG-HA-hAMDHD2 D294 (hAMDHD2 D294A). Cells were treated with 0.5 µg/ml TM for 48h (mean ± SEM, n=6, ** p<0.01, ns = not significant, One-way ANOVA Tukey post-test). **(E)** Genotyping results for the AMDHD2 deletion in dissected (E7-8) embryos and weaned mice. Figure supplements are available in Figure 2-figure supplements 1-3. Source data for this figure are available in Figure 2-source data 1-3.

Figure 3: Structural and biochemical characterization of human AMDHD2

(A) Influence of divalent addition (10 µM) on the stability of AMDHD2 in SEC buffer in thermal shift assays (mean + SEM, n=3, ns = not significant, *** p<0.0001 versus wildtype, one-way ANOVA). **(B)** Deacetylase activity of AMDHD2 in the presence of EDTA and several indicated divalents (mean + SEM, n=3, ns = not significant, * p<0.05, *** p<0.0001 versus wildtype, one-way ANOVA). **(C)** Overview of the human AMDHD2 dimer in cartoon representation. Monomer A is colored in gray and monomer B in blue. The two deacetylase domains are interacting with each other. The DUF domain is formed by residues of the N-terminus (light gray, light blue) and residues of the C-terminus (black, dark blue). GlcN6P (yellow sticks), Zn²⁺ (green sphere), and the putative active site lid (wheat) are highlighted. **(D)** Domains and secondary structure elements within one AMDHD2 monomer. The deacetylase domain (left) shows a TIM barrel-like fold, while the small DUF domain (right) is composed of a β-sandwich fold. α-helices are colored in blue, β-strands in red, and loops in gray. GlcN6P (yellow sticks) and Zn²⁺ (green sphere) are highlighted. **(E)** Close-up view of the active site in cartoon representation. Residues involved in ligand binding or catalysis are highlighted as sticks, as well as GlcN6P (yellow sticks), Zn²⁺ (green sphere) and two water molecules (red spheres). The GlcN6P binding site is formed by two deacetylase domains. Black dashed lines indicate key interactions to GlcN6P and green dashed lines the coordination of Zn²⁺. **(F)** Close-up view of the dimer interface in cartoon representation. His242, Arg243, and Ile280, which were mutated for further characterization of the dimer, are highlighted as sticks. **(G)** Representative chromatogram of an analytical size-exclusion chromatography of human AMDHD2 variants using a Superdex™ 200 Increase 10/300 GL column. Absorption at 280 nm (mAU: milli absorbance units) was plotted against the elution volume. **(H)** Molecular weight of human AMDHD2 based on analytical size-exclusion chromatography measurements (mean + SD, n=3.) **(I)** Deacetylase activity of wildtype (WT) and mutant human AMDHD2 (mean + SEM, n=6, *** p<0.0001 versus wildtype, one-way ANOVA). **(J)** Anomalous map of Zn²⁺ with a contour level of 5.0 RMSD (violet). Figure supplements are available in Figure 3-figure supplements 1-9. Source data for this figure are available in Figure 3-source data 1-5.

Figure 4: Characterization of AMDHD2 loss-of-function mutants

(A) SDS-gels stained with Coomassie brilliant blue of a representative bacterial test expression of the human AMDHD2 variants. The experiment was repeated three times with similar results. BI: before induction, AI: after induction, TL: total lysate, SN: soluble fraction/ supernatant. A band corresponding to the molecular weight of human AMDHD2 with His₆-tag (46 kDa) was present in all total lysates after induction. (B) Overview of the position of the potential loss-of-function mutations in human AMDHD2 in cartoon representation. GlcN6P (yellow sticks), the metal co-factor (green spheres), the active site Asp294 (violet sticks), and the eleven putative loss-of-function mutations (cyan sticks) are highlighted. (C) Deacetylase activity of wildtype (WT) and mutant human AMDHD2 (mean ± SEM, n=6, *** p<0.0001 versus wildtype, one-way ANOVA). Figure supplements are available in Figure 4-figure supplement 1. Source data for this figure are available in Figure 4-source data 1-5.

Figure 5: AMDHD2 limits HBP activity when GFPT2 replaces GFPT1 as the first enzyme

(A) Relative *GFPT1* and *GFPT2* mRNA levels (qPCR) in WT AN3-12 cells (mean ± SEM, n=4, *** p<0.001, unpaired t-test). (B) Western blot analysis of purified human GFPT1 and GFPT2 protein lysates of indicated cell lines. (C) Western blot analysis of AMDHD2 in indicated cell lines. (D) IC-MS analysis of UDP-GlcNAc levels in WT and AMDHD2 KO AN3-12 mESCs and N2a cells (mean ± SEM, n=5, *** p<0.001, one-way ANOVA). (E) Representative UDP-GlcNAc dose-response assay with hGFPT1 (black circle) and hGFPT2 (teal square) (mean ± SD, n=3). (F) Relative UDP-GlcNAc levels in indicated cell lines measured by IC-MS. Levels are normalized to those in AN3-12 mESCs (mean ± SEM, n≥3, *** p<0.001, one-way ANOVA). (G) Western blot analysis of O-GlcNAc-modified proteins (RL2), OGA, OGT, and tubulin in the indicated cell lines (H-J) Quantification of Western blot in (G) (mean ± SD, n=4, * p<0.05, ** p<0.01, *** p<0.001, ns = not significant, One-way ANOVA Dunnett post-test). Figure supplements are available in Figure 5-figure supplements 1-3. Source data for this figure are available in Figure 5-source data 1-25.

Figure 6: Differentiation of ESCs induces an enzymatic reconfiguration of the HBP by reducing the GFPT2:GFPT1 ratio

(A) Western blot analysis and quantification (mean ± SD, n=4, * p<0.05, unpaired t-test) of GFPT2 in WT AN3-12 control cells and upon partial differentiation by a 5-day LIF removal. (B) Relative *Gfpt2* mRNA level (qPCR) in WT AN3-12 cells and upon partial differentiation by a 5-day LIF removal (mean ± SEM, n=4, * p<0.05, unpaired t-test). (C) Relative *GFPT2/GFPT1* mRNA and

GFPT2/GFPT1 protein ratios in human ESCs and upon differentiation into cardiomyocytes (data obtained from: Frank et al. 2019, Bartsch et al. 2021). **(D)** Relative *GFPT2/GFPT1* mRNA and GFPT2/GFPT1 protein ratios in human ESCs and upon differentiation into neurons (data obtained from: Saez et al. 2018). **(E)** Model: Enzymatic configuration of the HBP in ESCs and somatic cells. The HBP (blue box) generates UDP-GlcNAc in multiple enzymatic steps. While ESCs mainly rely on GFPT2, more differentiated cells use GFPT1 for HBP entry. GFPT2 is less susceptible to UDP-GlcNAc inhibition than GFPT1 (indicated by red arrow). As an alternative regulatory mechanism ESCs require AMDHD2. Differentiation of ESCs induces an HBP reconfiguration, resulting in a decreased GFPT2:GFPT1 ratio. GFPT: glutamine fructose-6-phosphate amidotransferase, GNPDA: D-glucosamine-6-phosphate deaminase, GNA1: D-glucosamine-6-phosphate-Nacetyltransferase, AMDHD2: N-acetylglucosamine-6-phosphatedeacetylase, PGM3: phosphoglucomutase, UAP1: UDP-N-acetylglucosamine pyrophosphorylase. Figure supplements are available in Figure 6-figure supplement 1. Source data for this figure are available in Figure 6-source data 1-5.

List of Figure supplements

Figure 1-figure supplement 1

Figure 2-figure supplements 1-3

Figure 3-figure supplements 1-9

Figure 4-figure supplements 1

Figure 5-figure supplements 1-3

Figure 6-figure supplement 1

List of source data

Figure 1-source data 1: XTT assay of four TM resistant clones identified via insertional mutagenesis compared to control WT AN3-12 cells. (Figure 1C)

Figure 1-source data 2: anti-AMDHD2 Western Blot (raw) (Figure 1D)

Figure 1-source data 3: anti-AMDHD2 Western Blot (labelled) (Figure 1D)

Figure 1-source data 4: anti-Tubulin Western Blot (raw) (Figure 1D)

Figure 1-source data 5: anti-Tubulin Western Blot (labelled) (Figure 1D)

Figure 1-source data 6: Cell viability (XTT assay) of WT and AMDHD2 KO AN3-12 cells (Figure 1E)

Figure 1-figure supplement 1-source data 1: Cell viability (XTT assay) of WT AN3-12 cells and four TM resistant clones identified by chemical (ENU) mutagenesis (Figure 1- figure supplement 1A)

Figure 1-figure supplement 1-source data 2: Cell viability (XTT assay) of WT and two additional AMDHD2 KO AN3-12 cell lines (#2-3) (Figure 1- figure supplement 1D)

Figure 2-source data 1: IC-MS analysis of UDP-HexNAc levels of four TM resistant clones identified via insertional mutagenesis compared to control WT and AMDHD2 KO AN3-12 cells (Figure 2B)

Figure 2-source data 2: IC-MS analysis of UDP-GlcNAc levels of WT and AMDHD2 KO AN3-12 cells and both lines stably overexpressing FLAG-HA-hAMDHD2 and FLAG-HA-hAMDHD2 D294A respectively (Figure 2C)

Figure 2-source data 3: Cell viability (XTT assay) of WT and AMDHD2 KO AN3-12 cells and both lines stably overexpressing FLAG-HA-hAMDHD2 and FLAG-HA-hAMDHD2 D294A respectively (Figure 2D)

Figure 2-figure supplement 1-source data 1: IC-MS analysis of UDP-HexNAc levels of WT and two additional AMDHD2 KO AN3-12 cell lines (#2-3) (Figure 2-figure supplement 1)

Figure 2-figure supplement 2-source data 1: anti-AMDHD2 Western Blot (raw) (Figure 2-figure supplement 2A)

Figure 2-figure supplement 2-source data 2: anti-AMDHD2 Western Blot (labelled) (Figure 2-figure supplement 2A)

Figure 2-figure supplement 2-source data 3: anti-TUBULIN Western Blot (raw) (Figure 2-figure supplement 2A)

Figure 2-figure supplement 2-source data 4: anti-TUBULIN Western Blot (labelled) (Figure 2-figure supplement 2A)

Figure 2-figure supplement 2-source data 5: anti-FLAG Western Blot (raw) (Figure 2- figure supplement 2B)

Figure 2-figure supplement 2-source data 6: anti-FLAG Western Blot (labelled) (Figure 2-figure supplement 2B)

Figure 2-figure supplement 2-source data 7: anti-TUBULIN Western Blot (raw) (Figure 2-figure supplement 2B)

Figure 2-figure supplement 2-source data 8: anti-TUBULIN Western Blot (labelled) (Figure 2-figure supplement 2B)

Figure 3-source data 1: Thermal Shift Assay, melting temperatures of AMDHD2 in SEC buffer in the presence of varying divalents (Figure 3A)

Figure 3-source data 2: Deacetylase activity of AMDHD2 in the presence of EDTA and several indicated divalents (Figure 3B)

Figure 3- source data 3: Representative analytical size-exclusion chromatography of AMDHD2 variants (Figure 3G)

Figure 3-source data 4: Molecular weight of wildtype (WT) and mutant human AMDHD2 based on analytical size-exclusion chromatography measurements (Figure 3H)

Figure 3-source data 5: Deacetylase activity of wildtype (WT) and mutant human AMDHD2 (Figure 3I)

Figure 3-figure supplement 3-source data 1: Representative dynamic light scattering measurement of AMDHD2 (Figure 3-figure supplement 3)

Figure 3-figure supplement 9-source data 1: Deacetylase activity of human AMDHD2 towards GlcNAc6P, GalNAc6P, and GlcNAc6S

Figure 4-source data 1: First SDS-gel stained with Coomassie brilliant, provided as full raw unedited and labeled JPG files (Figure 4A)

Figure 4-source data 2: Second SDS-gel stained with Coomassie brilliant, provided as full raw unedited and labeled JPG files (Figure 4A)

Figure 4-source data 3: Third SDS-gel stained with Coomassie brilliant, provided as full raw unedited and labeled JPG files (Figure 4A)

Figure 4-source data 4: Fourth SDS-gel stained with Coomassie brilliant, provided as full raw unedited and labeled JPG files (Figure 4A)

Figure 4-source data 1-4: SDS-gels stained with Coomassie brilliant blue of a representative bacterial test expression of the human AMDHD2 variants in an Excel file (full raw unedited and labeled) (Figure 4A)

Figure 4-source data 5: Deacetylase activity of wildtype (WT) and mutant human AMDHD2 (Figure 4C)

Figure 4-figure supplement 1-source data 1: First SDS-gel stained with Coomassie brilliant, provided as full raw unedited and labeled JPG files (Figure 4-figure supplement 1)

Figure 4-figure supplement 1-source data 2: Second SDS-gel stained with Coomassie brilliant, provided as full raw unedited and labeled JPG files (Figure 4-figure supplement 1)

Figure 4- figure supplement 1-source data 1-2: SDS-gels stained with Coomassie brilliant blue of a representative bacterial test expression of the human AMDHD2 variants in an Excel file (full raw unedited and labeled) (Figure 4-figure supplement 1)

Figure 5-source data 1: Relative *GFPT1* and *GFPT2* mRNA levels (qPCR) in WT AN3-12 cells (Figure 5A)

Figure 5-source data 2: anti-GFPT1 Western Blot (raw) (Figure 5B)

Figure 5-source data 3: anti-GFPT1 Western Blot (labelled) (Figure 5B)

Figure 5-source data 4: anti-Tubulin Western Blot (raw) (Figure 5B)

Figure 5-source data 5: anti-Tubulin Western Blot (labelled) (Figure 5B)

Figure 5-source data 6: anti-GFPT2 Western Blot (raw) (Figure 5B)

Figure 5-source data 7: anti-GFPT2 Western Blot (labelled) (Figure 5B)

Figure 5-source data 8: anti-Tubulin Western Blot (raw) (Figure 5B)

Figure 5-source data 9: anti-Tubulin Western Blot (labelled) (Figure 5B)

Figure 5-source data 10: anti-AMDHD2 Western Blot (raw) (Figure 5C)

Figure 5-source data 11: anti-AMDHD2 Western Blot (labelled) (Figure 5C)

Anti-TUBULIN: same as Figure 5- source data 4 (Figure 5C)

Anti-TUBULIN: same as Figure 5- source data 5 (Figure 5C)

Figure 5-source data 12: IC-MS analysis of UDP-GlcNAc levels of AMDHD2 KO compared to WT cells (Figure 5D)

Figure 5-source data 13: UDP-GlcNAc dose-response assay with hGFPT1 and hGFPT2 (Figure 5E)

Figure 5-source data 14: Relative UDP-GlcNAc levels in indicated cell lines measured by IC-MS (Figure 5F)

Figure 5-source data 15: anti-RL2 Western Blot (raw) (Figure 5G)

Figure 5-source data 16: anti-RL2 Western Blot (labelled) (Figure 5G)

Figure 5-source data 17: anti-OGA Western Blot (raw) (Figure 5G)

Figure 5-source data 18: anti-OGA Western Blot (labelled) (Figure 5G)

Figure 5-source data 19: anti-OGT Western Blot (raw) (Figure 5G)

Figure 5-source data 20: anti-OGT Western Blot (labelled) (Figure 5G)

Figure 5-source data 21: anti-TUBULIN Western Blot (raw) (Figure 5G)

Figure 5-source data 22: anti-TUBULIN Western Blot (labelled) (Figure 5G)

Figure 5-source data 23: Quantification of O-GlcNAc modified proteins (RL2) (Figure 5H)

Figure 5-source data 24: Quantification of OGA expression (Figure 5I)

Figure 5-source data 25: Quantification of OGT expression (Figure 5J)

Figure 5-figure supplement 1-source data 1: Relative UDP-GlcNAc levels of distinct mutants compared to WT AN3-12 mESCs (Figure 5-figure supplement 1)

Figure 5-figure supplement 2-source data 1: anti-AMDHD2 Western Blot (raw) (Figure 5-figure supplement 2A)

Figure 5-figure supplement 2-source data 2: anti-AMDHD2 Western Blot (labelled) (Figure 5-figure supplement 2A)

Figure 5-figure supplement 2-source data 3: anti-TUBULIN Western Blot (raw) (Figure 5-figure supplement 2A)

Figure 5-figure supplement 2-source data 4: anti-TUBULIN Western Blot (labelled) (Figure 5-figure supplement 2A)

Figure 5-figure supplement 2-source data 5: IC-MS analysis of UDP-GlcNAc levels of WT and AMDHD2 KO C2C12 myoblasts (Figure 5-figure supplement 2B)

Figure 5-figure supplement 3-source data 1: L-Gln kinetic of WT human GFPT1 and WT human GFPT2 (Figure 5-figure supplement 3A)

Figure 5-figure supplement 3-source data 2: Fructose-6-Phosphate kinetic of WT human GFPT1 and WT human GFPT2 (Figure 5-figure supplement 3B)

Figure 6-source data 1: anti-GFPT2 Western Blot (raw) (Figure 6A)

Figure 6-source data 2: anti-GFPT2 Western Blot (labelled) (Figure 6A)

Figure 6-source data 3: anti-TUBULIN Western Blot (raw) (Figure 6A)

Figure 6-source data 4: anti-TUBULIN Western Blot (labelled) (Figure 6A)

Figure 6-source data 5: Relative *Gfpt2* mRNA level (qPCR) in WT AN3-12 cells and upon partial differentiation by a 5-day LIF removal (-Lif) (Figure 6B)

Figure 6-figure supplement 1-source data 1: Relative *Nanog* and *Klf4* mRNA level (qPCR) in WT AN3-12 cells and upon partial differentiation by a 5-day LIF removal (-Lif) (Figure 6-figure supplement 6A)

Figure 6-figure supplement 1-source data 2: Relative *Gfpt1* and *Amdhd2* mRNA level (qPCR) in WT AN3-12 cells and upon partial differentiation by a 5-day LIF removal (-Lif) (Figure 6-figure supplement 6B)

Figure 6-figure supplement 1-source data 3: anti-GFPT1 Western Blot (raw) (Figure 6-figure supplement 6C)

Figure 6-figure supplement 1-source data 4: anti-GFPT1 Western Blot (labelled) (Figure 6-figure supplement 6C)

Figure 6-figure supplement 1-source data 5: anti-AMDHD2 Western Blot (raw) (Figure 6-figure supplement 6C)

Figure 6-figure supplement 1-source data 6: anti-AMDHD2 Western Blot (labelled) (Figure 6-figure supplement 6C)

Figure 6-figure supplement 1-source data 7: anti-TUBULIN Western Blot (raw) (Figure 6-figure supplement 6C)

Figure 6-figure supplement 1-source data 8: anti-TUBULIN Western Blot (labelled) (Figure 6-figure supplement 6C)

Figure 6-figure supplement 1-source data 9: Quantification of GFPT1 expression (Figure 6-figure supplement 6D)

Figure 6-figure supplement 1-source data 10: Quantification of AMDHD2 expression (Figure 6-figure supplement 6D)

1505 **Table 1 – Data collection and refinement statistics of human AMDHD2**

| | AMDHD2 + Zn + GlcN6P | AMDHD2 + Zn |
|---------------------------------------|------------------------------------------------|------------------------------------------------|
| Wavelength (Å) | 1.00 | 1.00 |
| Resolution range (Å) | 45.71 - 1.90 (1.97 - 1.90) | 48.21 - 1.84 (1.90 - 1.84) |
| Space group | P 2 ₁ 2 ₁ 2 ₁ | P 2 ₁ 2 ₁ 2 ₁ |
| a, b, c (Å) | 63.3 161.4 86.6 | 61.8 84.3 154.2 |
| α, β, γ (°) | 90 90 90 | 90 90 90 |
| Total reflections | 428727 (42693) | 468961 (46539) |
| Unique reflections | 70760 (6907) | 71036 (6953) |
| Multiplicity | 6.1 (6.2) | 6.6 (6.7) |
| Completeness (%) | 99.7 (98.3) | 99.9 (99.2) |
| Mean I/sigma(I) | 11.46 (1.16) | 12.53 (1.06) |
| Wilson B-factor | 34.7 | 29.7 |
| R_{merge} (%) | 9.5 (140.4) | 10.2 (150.6) |
| R_{meas} (%) | 10.4 (153.3) | 11.0 (163.3) |
| R_{pim} (%) | 4.2 (60.9) | 4.3 (62.5) |
| CC_{1/2} (%) | 99.9 (49.4) | 99.9 (49.9) |
| CC* (%) | 100 (81.3) | 100 (81.6) |
| Reflections used in refinement | 70751 (6906) | 71024 (6952) |
| Reflections used for R-free | 1980 (194) | 1992 (195) |
| R_{work} (%) | 18.5 (31.7) | 18.2 (31.2) |
| R_{free} (%) | 21.3 (29.6) | 20.6 (33.6) |
| CC_{work} (%) | 96.6 (73.4) | 96.6 (75.7) |
| CC_{free} (%) | 94.4 (73.1) | 95.4 (72.8) |
| Number of non-hydrogen atoms | 6361 | 6331 |
| macromolecules | 5997 | 5999 |
| ligands | 34 | 14 |
| solvent | 330 | 318 |
| Protein residues | 801 | 798 |
| RMS (bonds) (Å) | 0.005 | 0.004 |
| RMS (angles) (°) | 0.69 | 0.70 |
| Ramachandran favored (%) | 96.9 | 97.1 |
| Ramachandran allowed (%) | 2.9 | 2.7 |
| Ramachandran outliers (%) | 0.25 | 0.25 |
| Rotamer outliers (%) | 0.32 | 0.32 |
| Clashscore | 0.67 | 0.92 |
| Average B-factor | 43.59 | 37.67 |
| macromolecules | 43.81 | 37.76 |
| ligands | 40.19 | 41.98 |
| solvent | 40.10 | 35.72 |
| Number of TLS groups | 4 | 4 |
| PDB ID | 7NUT | 7NUU |

1506 Statistics for the highest-resolution shell are shown in parentheses.
1507
1508

Table 2 – Kinetic parameters of human GFPT1 and GFPT2

| | L-Glu production | | | D-GlcN6P production | | | UDP-GlcNAc inhibition |
|-------------------------------------------------|---------------------|---------------------------------|------------------------------------------------------|---------------------|---------------------------------|------------------------------------------------------|--------------------------|
| | K_m L-Gln [mM] | k_{cat} [s ⁻¹] | k_{cat}/K_m [mM ⁻¹ s ⁻¹] | K_m Frc6P [mM] | k_{cat} [s ⁻¹] | k_{cat}/K_m [mM ⁻¹ s ⁻¹] | IC ₅₀ [μM] |
| GFPT1 | 1.1 ± 0.19 | 3.6 ± 0.18 | 3.3 | 0.08 ± 0.01 | 1.7 ± 0.09 | 21.3 | 57.0 -8.3/+9.7 |
| GFPT2 | 0.5 ± 0.06 | 3.7 ± 0.10 | 7.4 | 0.29 ± 0.05 | 1.8 ± 0.09 | 6.2 | 367.3 -43.6/+49.5 |
| Unpaired t-test (two- sided) | ** p=0.005 | | | ** p=0.0027 | | | *** p=0.0002 |

Figure supplement legends

Figure 1-figure supplements | Chemical mutagenesis screen for tunicamycin resistance in haploid mESCs identifies AMDHD2

Figure 1-figure supplement 1, Identification and confirmation of AMDHD2 as the causative gene for mediating TM resistance by elevated UDP-GlcNAc levels. **(A)** Representative cell viability (XTT assay) of WT AN3-12 mESCs and four TM resistant clones (clone A-D) identified by the chemical (ENU) mutagenesis and that were used for whole exome sequencing. Cells were treated with 0.5 µg/ml TM for 48h. **(B)** Table listing all mutations in the *Amdhd2* locus identified in the TM resistance screen. **(C)** Schematic representation of experimental workflow for TM resistance screen using retroviral-based gene trap insertional mutagenesis. **(D)** Cell viability (XTT assay) of WT and two additional AMDHD2 KO AN3-12 cell lines (#2-3), generated with distinct guide combinations. Cells were treated with 0.5 µg/ml TM for 48h (mean ± SEM, n=6, *** p<0.001, One-way ANOVA Dunnett post-test).

Figure 2-figure supplements | Disruption of *Amdhd2* mediates tunicamycin resistance via elevated HBP flux

Figure 2-figure supplement 1, AMDHD2 disruption in AN3-12 mESCs increases HBP flux.

UDP-HexNAc concentration of the two additional AMDHD2 KO cell lines (#2-3), generated with distinct guide combinations compared to WT AN3-12 mESCs (mean \pm SEM, $n \geq 3$, *** $p < 0.001$, one-way ANOVA). UDP-HexNAc is the combined pool of the UDP-GlcNAc and UDP-GalNAc epimer pools.

Figure 2-figure supplement 2, Generation of different AN3-12 mESC lines stably over-expressing WT FLAG-HA-hAMDHD2 and mutant FLAG-HA-hAMDHD2 D294A protein. **(A)** Western blot analysis of AMDHD2 expression in WT and AMDHD2 KO AN3-12 cells expressing WT FLAG-HA-hAMDHD2 (hAMDHD2) and mutant FLAG-HA-hAMDHD2 D294A (hAMDHD2 D294A). The asterisk (*) indicates the band for the recombinant WT FLAG-HA-hAMDHD2 and mutant FLAG-HA-hAMDHD2 D294A protein. The lower band deemed to be a mixture of endogenous mAMDHD2 and recombinant hAMDHD2/ hAMDHD2 D294A protein upon cleavage of the N-terminal FLAG-HA-tag. **(B)** Western blot analysis of FLAG expression in WT and AMDHD2 KO AN3-12 cells expressing WT FLAG-HA-hAMDHD2 (hAMDHD2) and mutant FLAG-HA-hAMDHD2 D294A (hAMDHD2 D294A).

Figure 2-figure supplement 3, Generation of AMDHD2 KO founder mice. **(A)** Schematic representation of the CRISPR/Cas9-targeted exon of the mouse *Amdhd2* locus. Deletions in founder lines 1-4 are indicated in red. **(B)** Table listing used guide combinations and deletion details of the AMDHD2 KO founder lines. **(C)** Representative genotyping results of heterozygous AMDHD2 KO mice. The WT PCR product is 675 bp and the *Amdhd2* KO allele shows a size of 300 bp (mouse line 1).

Figure 3-figure supplements | Structural and biochemical characterization of human AMDHD2

Figure 3-figure supplement 1, Stereo image of the human AMDHD2 dimer in cartoon representation. Monomer A is colored in gray and monomer B in blue. The two deacetylase domains are interacting with each other. The DUF domain is formed by residues of the N-terminus (light gray, light blue) and residues of the C-terminus (black, dark blue). GlcN6P (yellow sticks), Zn^{2+} (green sphere), and the putative active site lid (wheat) are highlighted.

Figure 3-figure supplement 2, B-factor representation of WT human AMDHD2. The protein is presented as putty cartoon and colored from low to high B-factors (24-108 Å², blue to red).

Figure 3-figure supplement 3, **Oligomeric state of human AMDHD2.** Representative DLS measurement of WT AMDHD2. Table: Parameters of the representative DLS measurement showing a dimeric assembly.

Figure 3-figure supplement 4, Superposition of GlcN6P-bound AMDHD2 monomer A (gray) and monomer B (blue) in cartoon representation. GlcN6P (yellow sticks) and Zn^{2+} (green spheres) are highlighted.

Figure 3-figure supplement 5, Close-up view of the active site in cartoon representation. Residues involved in ligand binding or catalysis are highlighted as sticks, as well as GlcN6P (yellow sticks), Zn^{2+} (green sphere) and two water molecules (red spheres). Three antiparallel β -strands (β 15- β 17, colored wheat) build a β -sheet close to the active site.

Figure 3-figure supplement 6, Superposition of the structures of GlcN6P-bound (gray, blue) and GlcN6P-free (green, red) human AMDHD2 with RMSD of 0.67 Å over 792 main chain residues in cartoon representation. GlcN6P (yellow sticks) and Zn^{2+} (green spheres) are highlighted.

Figure 3-figure supplement 7, Active site of human AMDHD2. **(A)** Omit map of the active site of human AMDHD2 in cartoon representation. Residues involved in ligand binding or catalysis are highlighted as sticks, as well as GlcN6P (yellow sticks). The Fo-Fc omit map is colored in green and its contour level is at 1.5 RMSD. **(B)** 2D ligand-protein interaction diagram of GlcN6P interacting with human AMDHD2. Ligand bonds are colored in gray and amino acid side chain bonds in black. Green dashed lines indicate hydrogen bonds and red spiked arcs present residues making non-bonded contacts with the ligands.

Figure 3-figure supplement 8, Protein sequence alignment of AMDHD2. Red boxes indicate identical residues, red letters indicate similar residues. The deacetylase domain and secondary structure elements are annotated, as well as the positions of insertions and extensions in AMDHD2 isoform 2 and isoform 3. Residues involved in

product binding, catalysis, or metal binding are highlighted. The putative active site lid is marked. Moreover, the positions of the potential loss-of-function mutations and the control mutations are labeled.

Figure 3-figure supplement 9, Deacetylase activity of human AMDHD2 towards GlcNAc6P, GalNAc6P, and GlcNAc6S (mean + SEM, n=6, *** p<0.0001 versus GlcNAc6P, one-way ANOVA).

Figure 4-figure supplements | Characterization of AMDHD2 loss-of-function mutants

Figure 4-figure supplement 1, SDS-gels stained with Coomassie brilliant blue of a representative bacterial test expression of the human AMDHD2 variants. The experiment was repeated three times with similar results. BI: before induction, AI: after induction, TL: total lysate, SN: soluble fraction/ supernatant, PL: pellet fraction solubilized in 8 M urea.

Figure 5-figure supplements | AMDHD2 limits HBP activity when GFPT2 replaces GFPT1 as the first enzyme

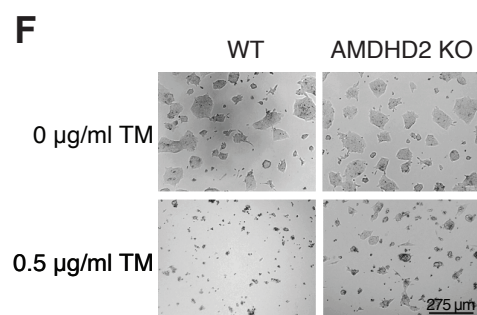
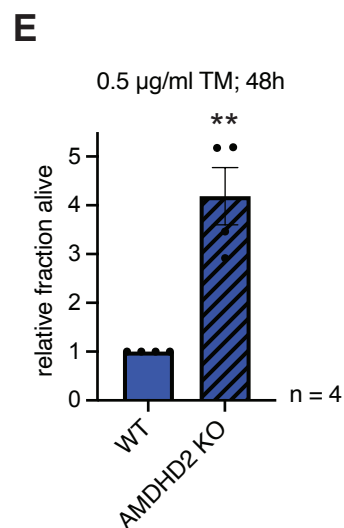
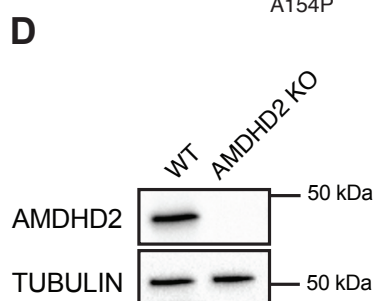
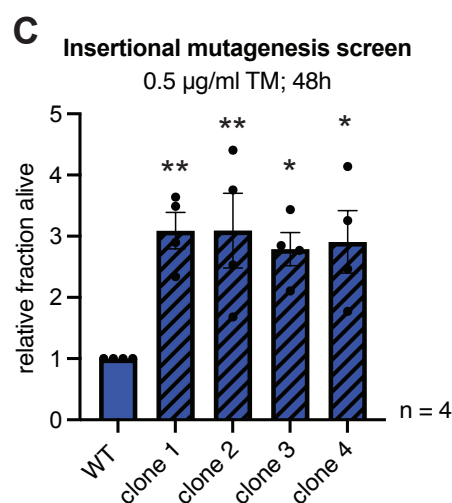
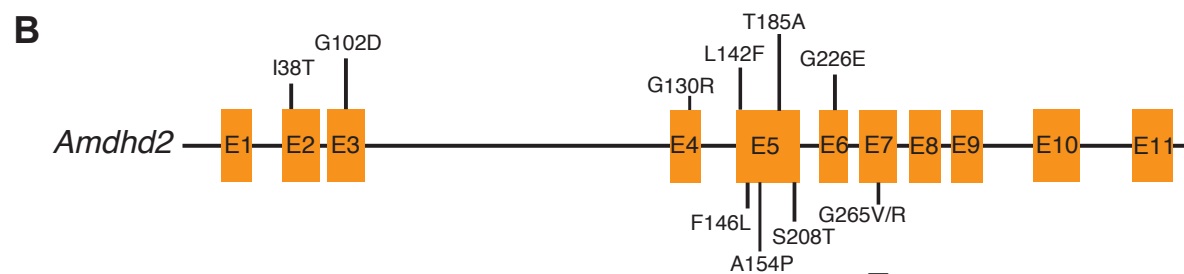
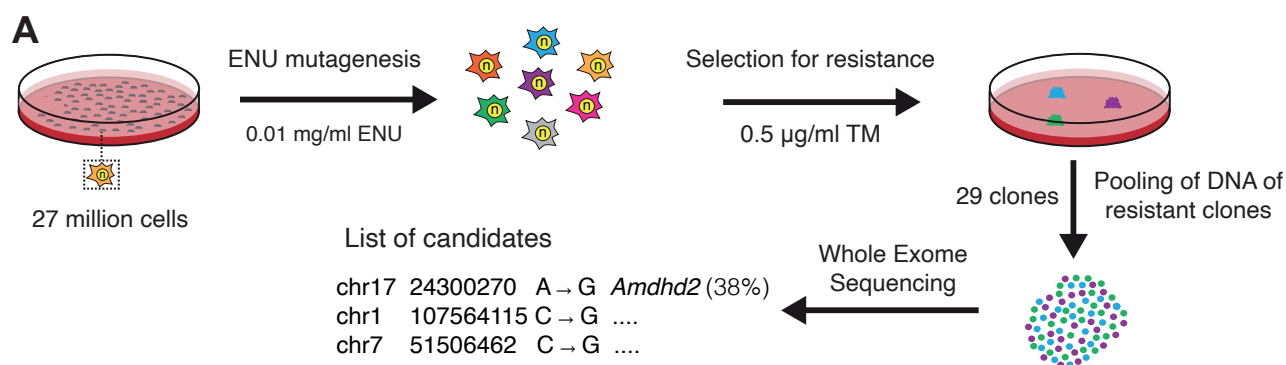
Figure 5-figure supplement 1, Manipulation of GFPT1 in AN3-12 cells has no influence on UDP-GlcNAc levels. IC-MS analysis of relative UDP-GlcNAc levels of WT, GFPT1 G451E, GFPT1 KO and AMDHD2 KO AN3-12 cells. (mean \pm SEM, n=7, *** p<0.001, one-way ANOVA Dunnett post-test)

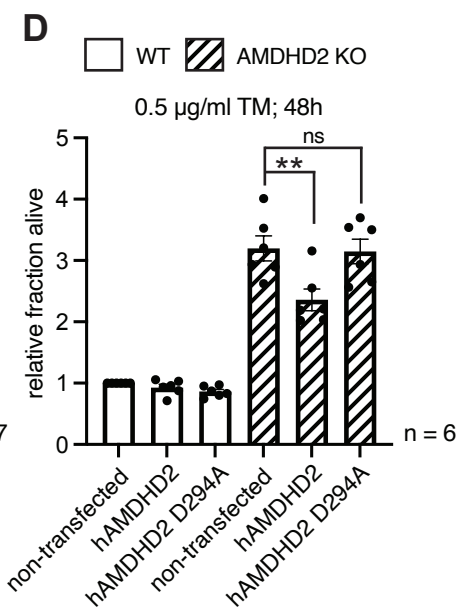
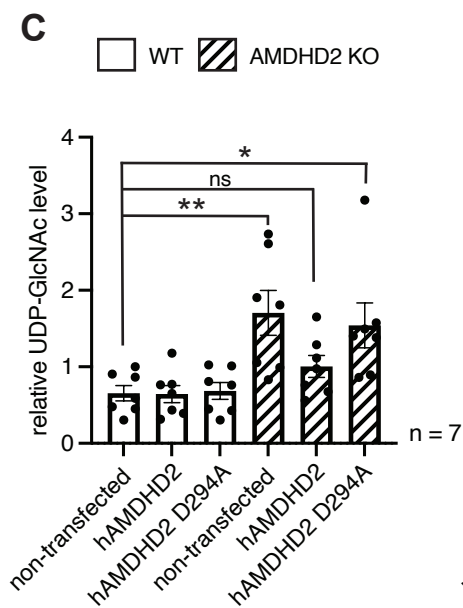
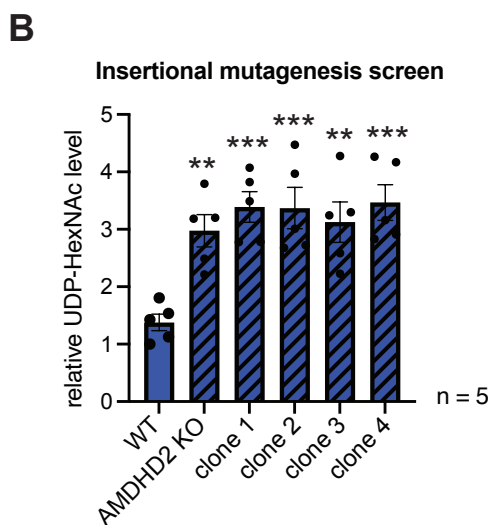
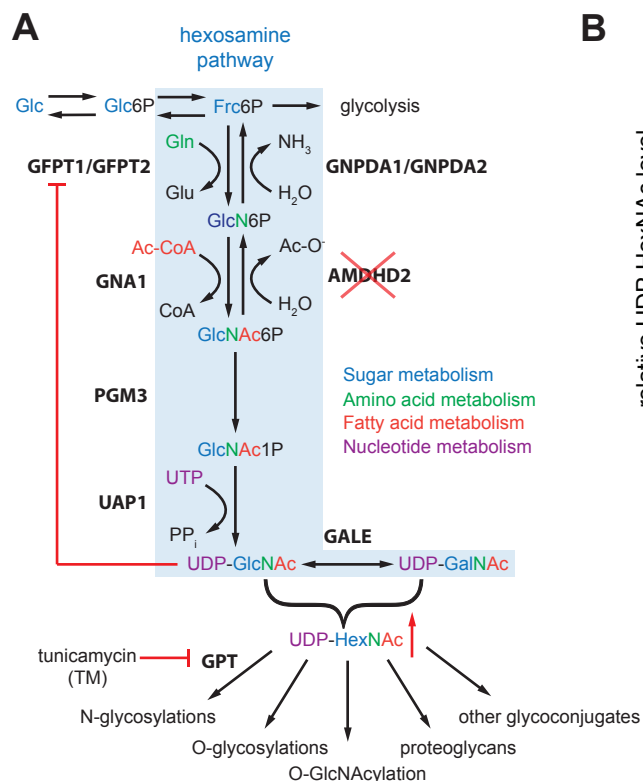
Figure 5-figure supplement 2, Deletion of AMDHD2 has no effect on HBP flux in C2C12 myoblasts. **(A)** Western blot analysis of AMDHD2 expression in two AMDHD2 KO lines (clone 1-2) compared to WT C2C12 myoblasts. **(B)** IC-MS analysis of relative UDP-GlcNAc levels of two AMDHD2 KO lines (clone 1-2) compared to WT C2C12 myoblasts (mean \pm SEM, n=6, ns = not significant, one-way ANOVA Dunnett post-test).

Figure 5-figure supplement 3, Biochemical characterization of human GFPT2 compared to human GFPT1. **(A)** L-Gln kinetic of WT human GFPT1 (black circle) and WT human GFPT2 (teal square) (mean \pm SEM, hGFPT1 n=5, hGFPT2 n=4). **(B)** Frc6P kinetic of WT hGFPT1 (black circle) and WT hGFPT2 (teal square) (mean \pm SEM, hGFPT1 n=5, hGFPT2 n=8).

Figure 6-figure supplements | Differentiation of ESCs induces an enzymatic reconfiguration of the HBP by reducing the GFPT2:GFPT1 ratio

Figure 6-figure supplement 1, The effect of partial differentiation upon LIF removal in AN3-12 cells on the enzymatic HBP composition. **(A)** Relative *Nanog* and *Klf4* mRNA-level (qPCR) of WT AN3-12 cells and upon partial differentiation by 5 days of LIF removal (SEM \pm n=4, ns = not significant, unpaired t-test). **(B)** Relative *Gfpt1* and *Amdhd2* mRNA-level (qPCR) of WT AN3-12 cells and upon partial differentiation by 5 days of LIF removal (mean \pm SEM, n=4, ns = not significant, unpaired t-test). **(C)** Representative Western blot analysis of GFPT1 and AMDHD2 in WT AN3-12 cells and upon partial differentiation by 5 days of LIF removal. **(D)** Quantification of Western blot as shown in (C) (mean \pm SD, n=4, ns = not significant, unpaired t-test).





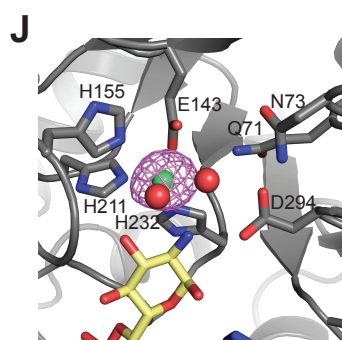
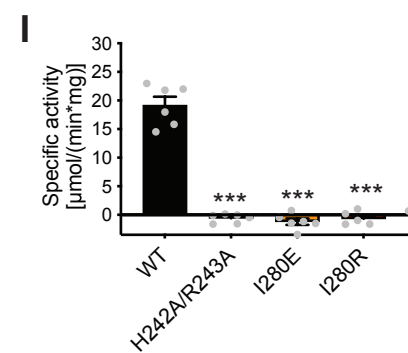
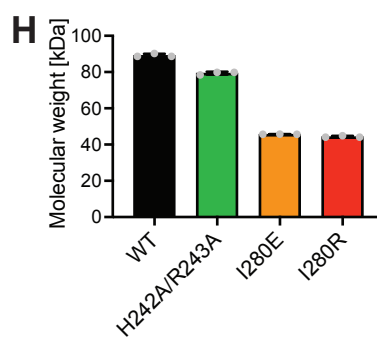
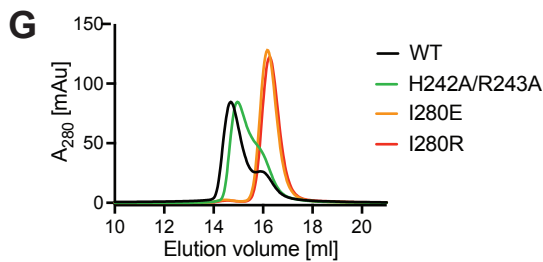
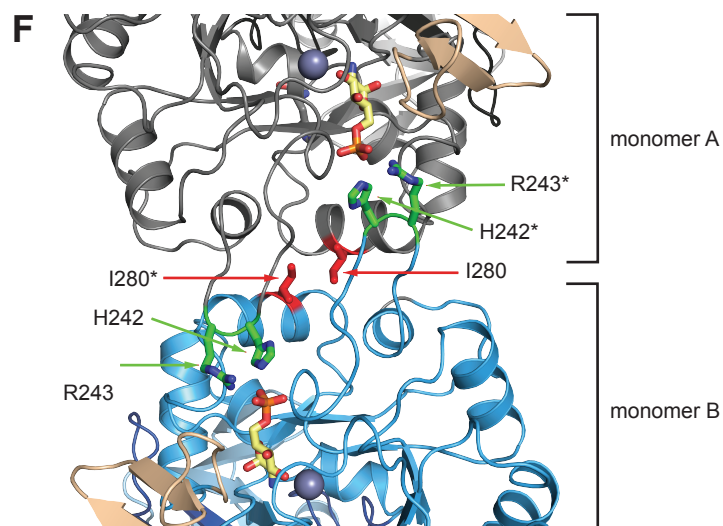
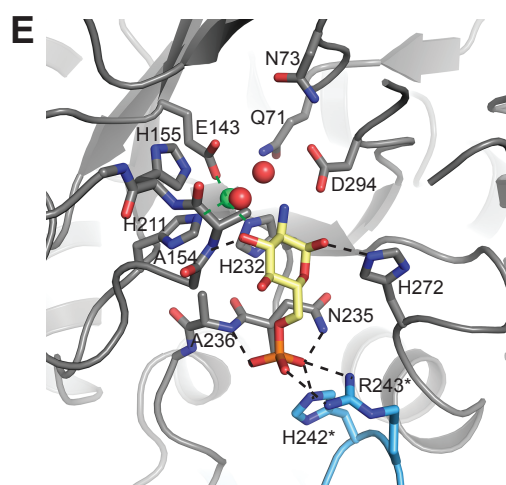
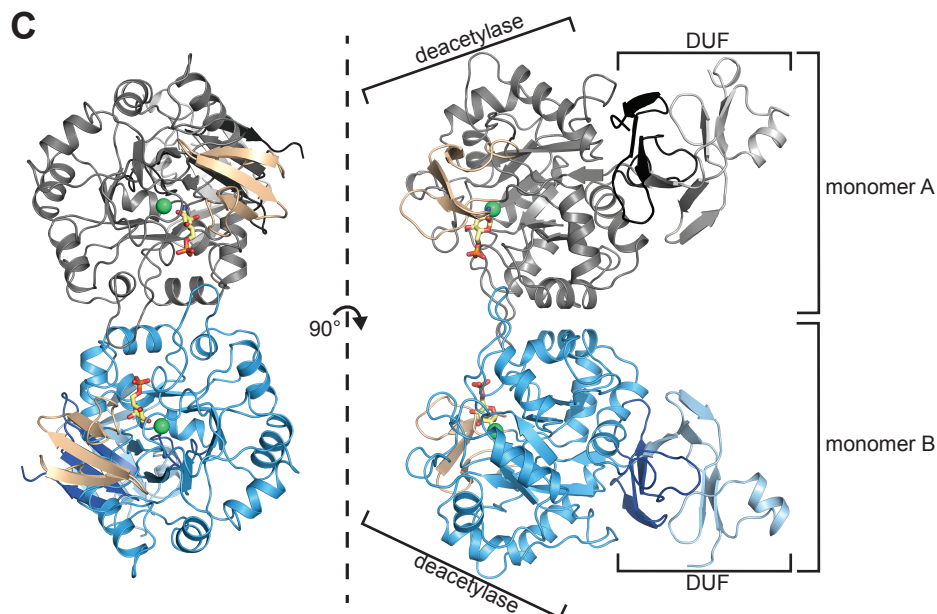
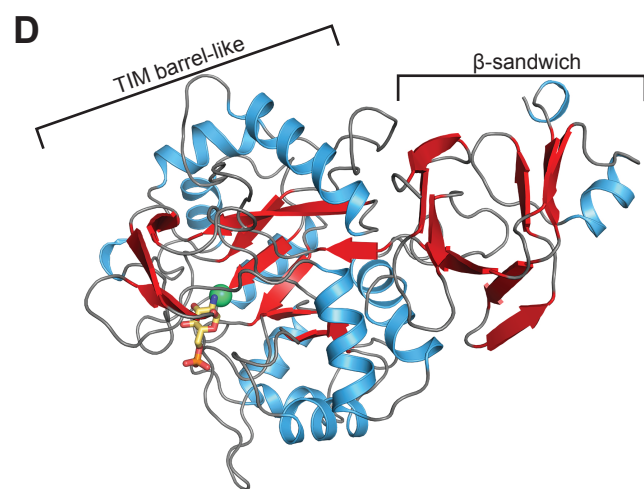
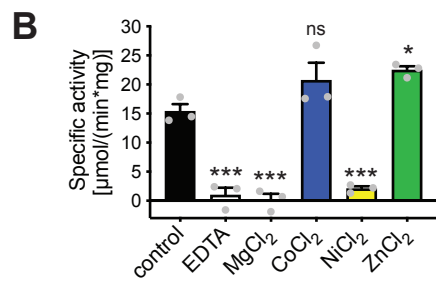
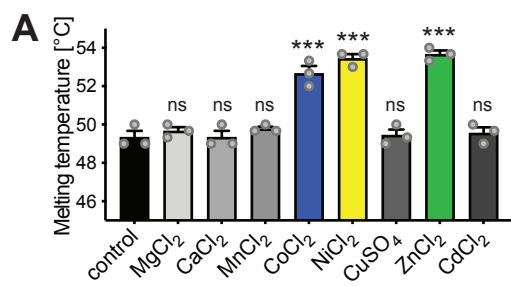
E

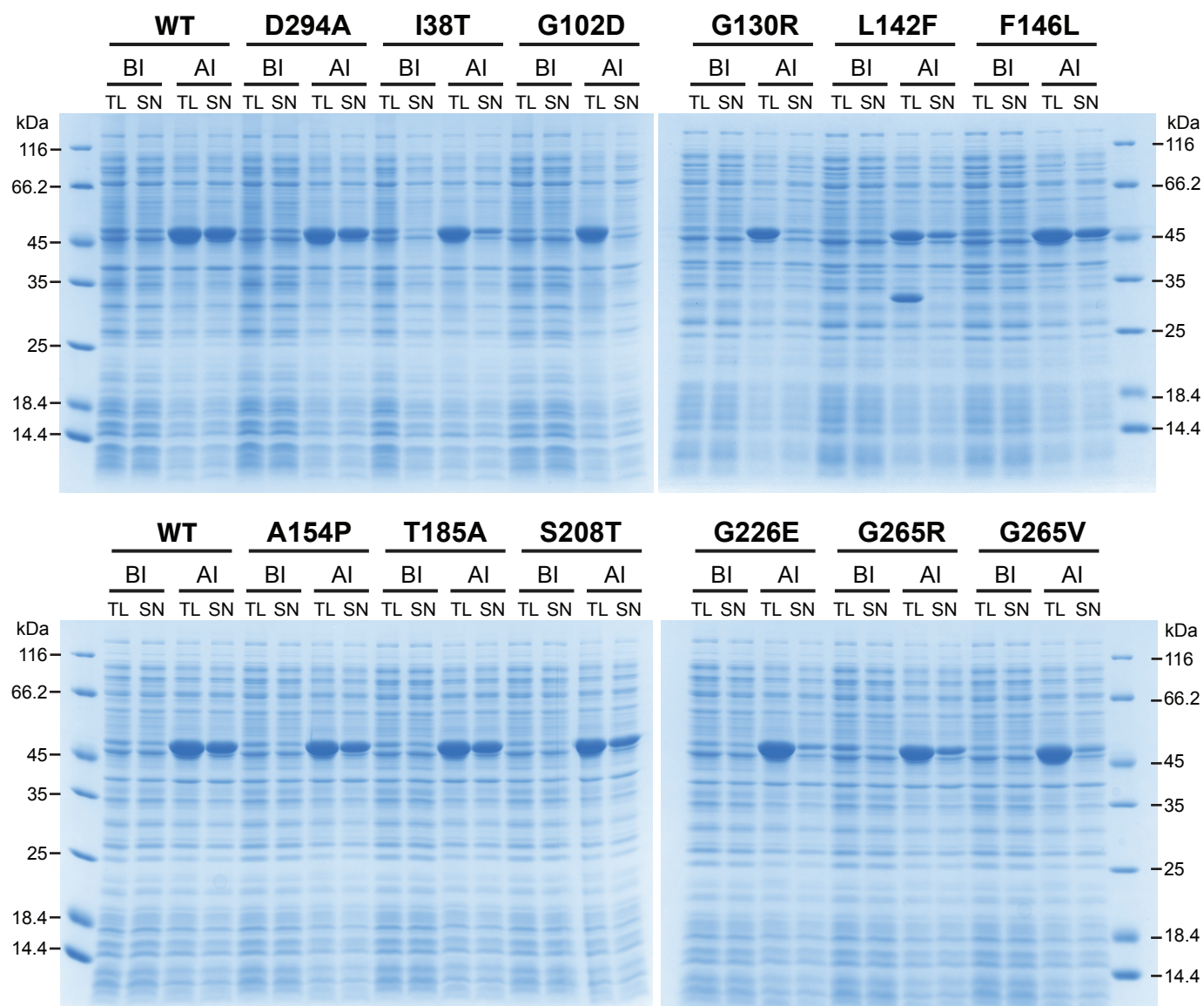
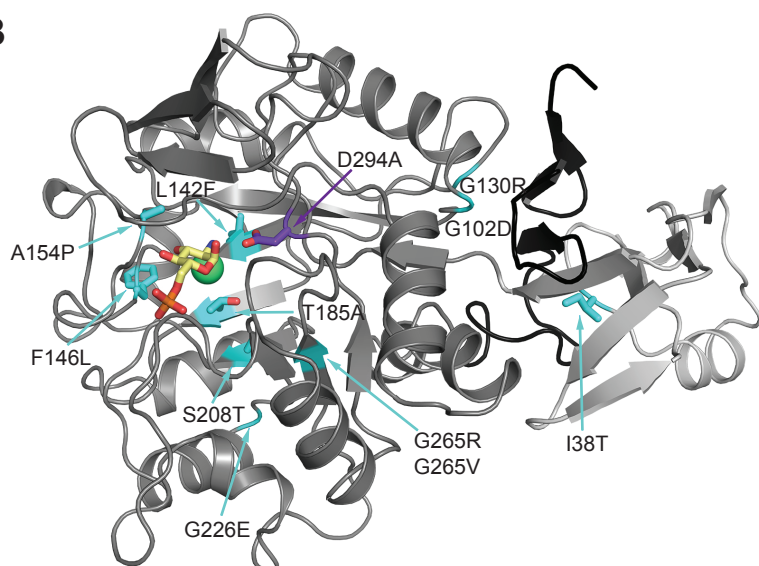
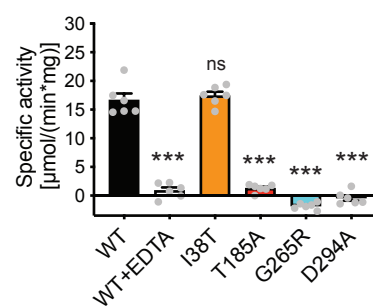
Prenatal dissection

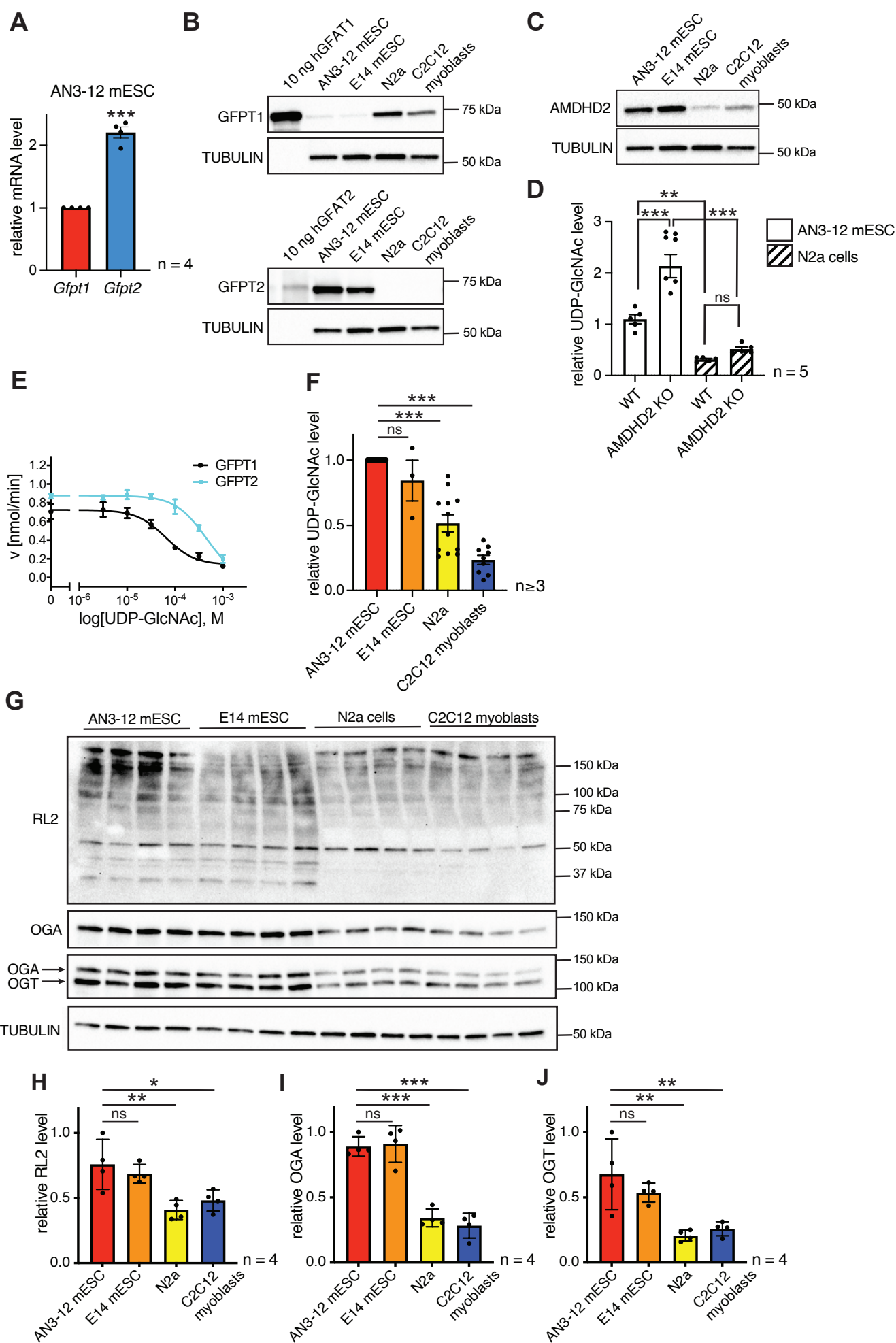
| Genotype | No. of mice | % |
|-----------------------|-------------|-----|
| WT | 10 | 22 |
| AMDHD2 ^{+/-} | 25 | 54 |
| AMDHD2 ^{-/-} | 11 | 24 |
| Total | 46 | 100 |

Postnatal

| Genotype | No. of mice | % |
|-----------------------|-------------|-----|
| WT | 56 | 54 |
| AMDHD2 ^{+/-} | 48 | 46 |
| AMDHD2 ^{-/-} | 0 | 0 |
| Total | 104 | 100 |



A**B****C**



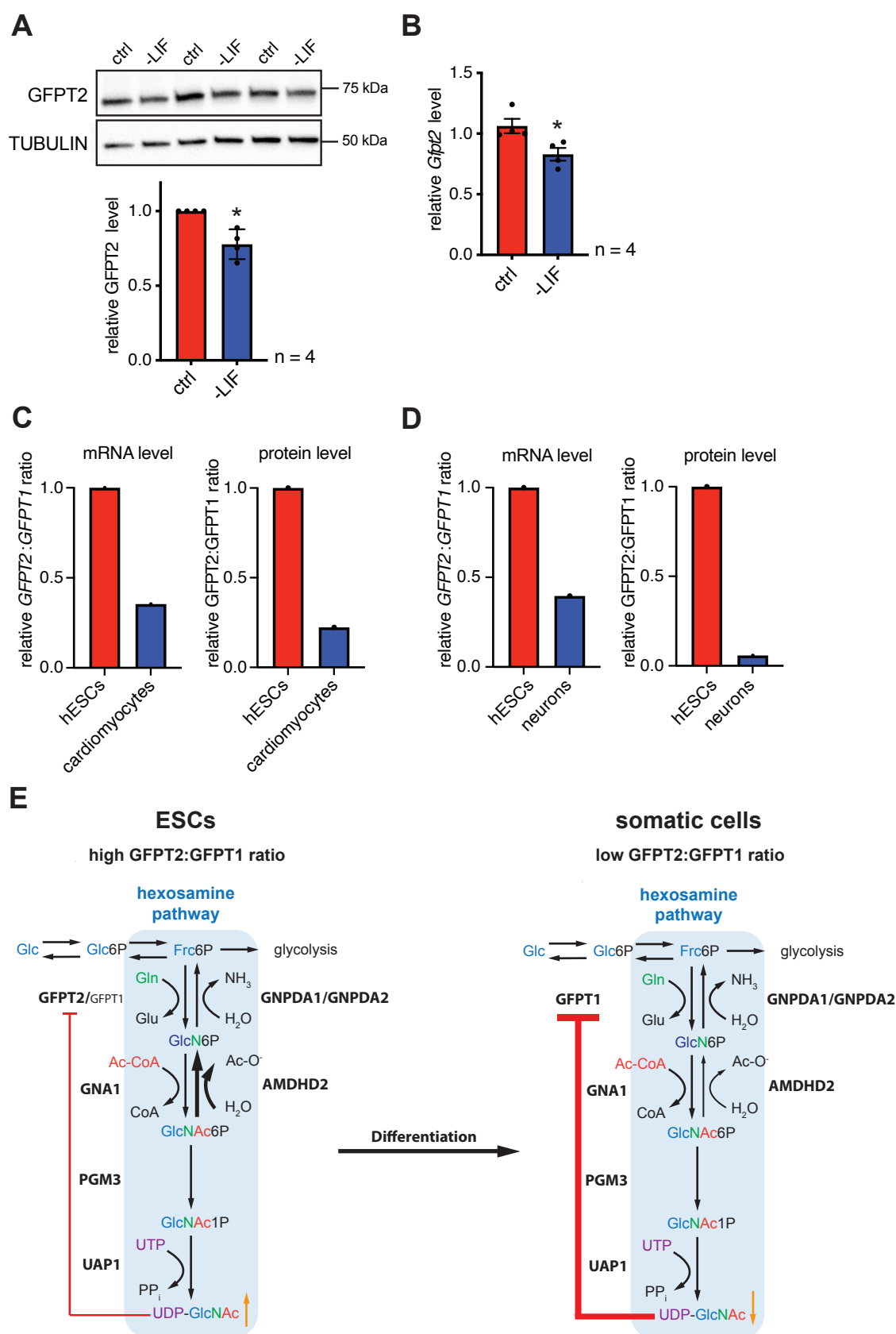


Figure 1-figure supplement 1

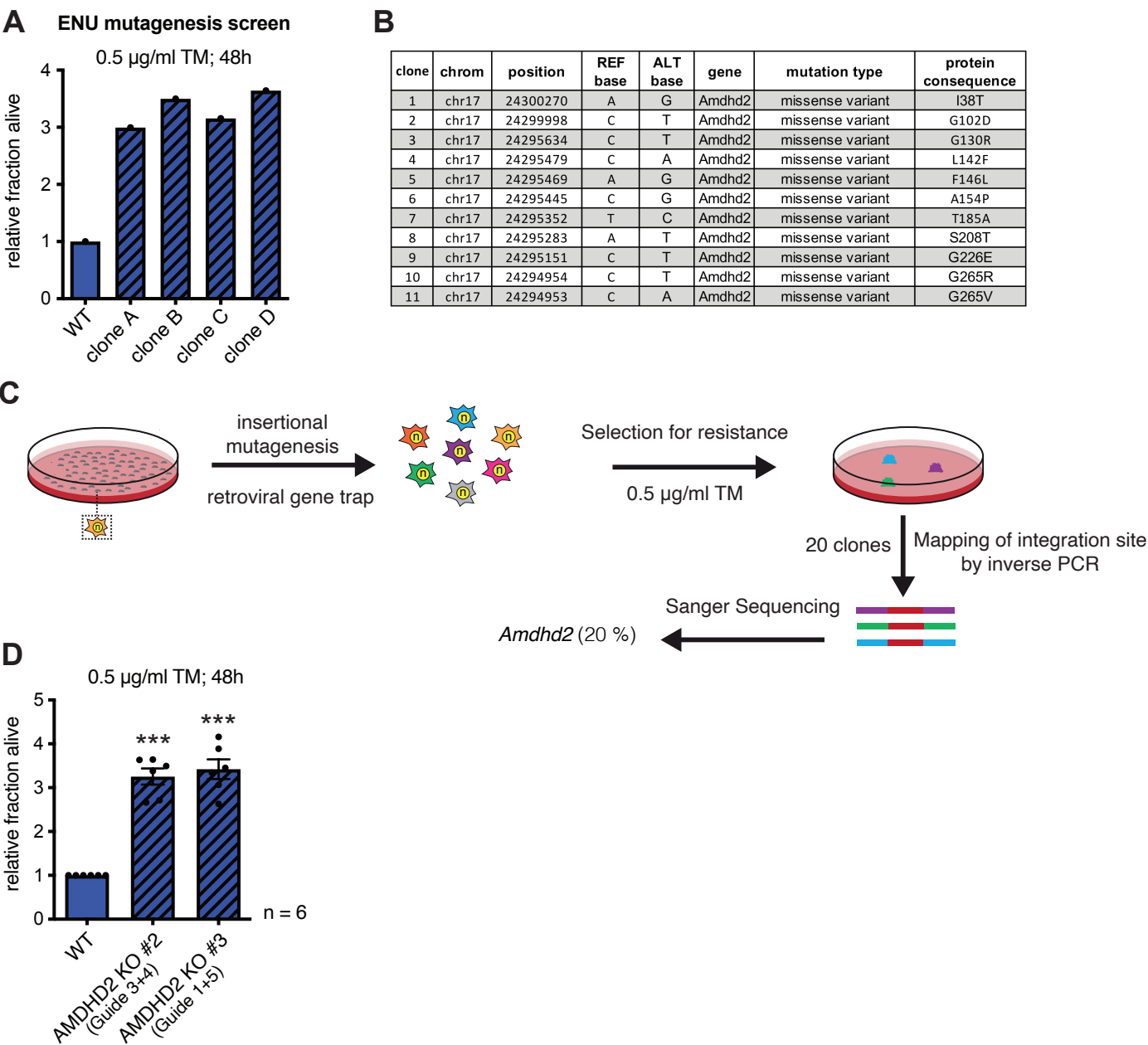


Figure 2-figure supplement 1

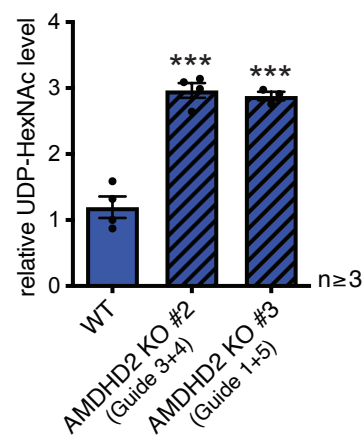


Figure 2-figure supplement 2

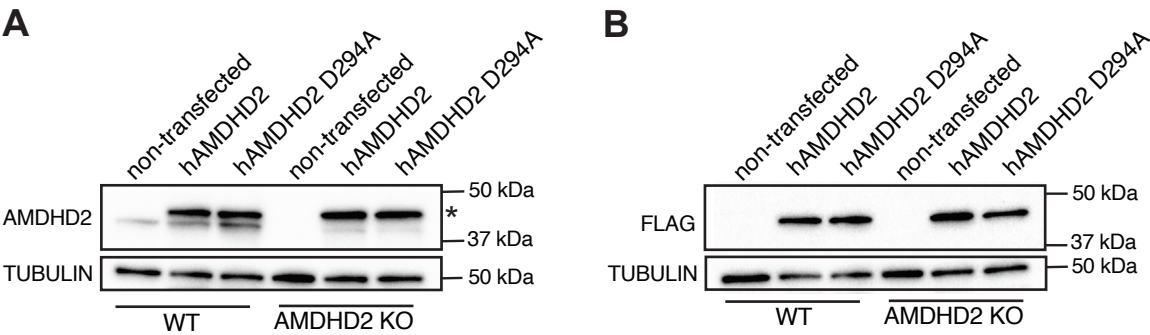


Figure 2-figure supplement 3

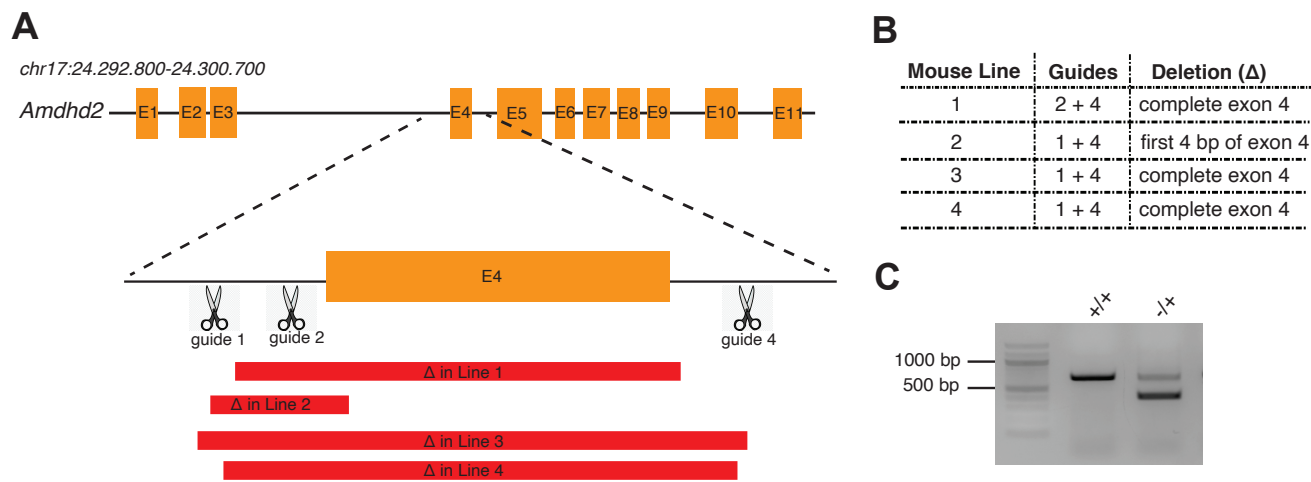


Figure 3-figure supplement 1

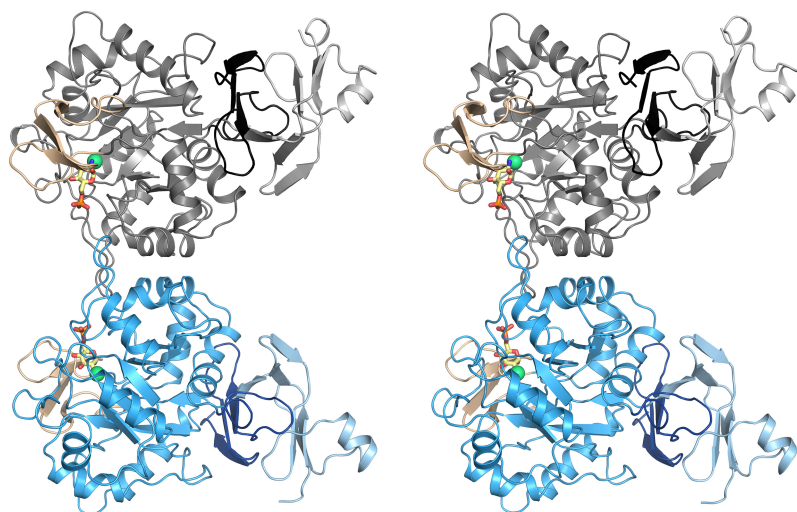


Figure 3-figure supplement 2

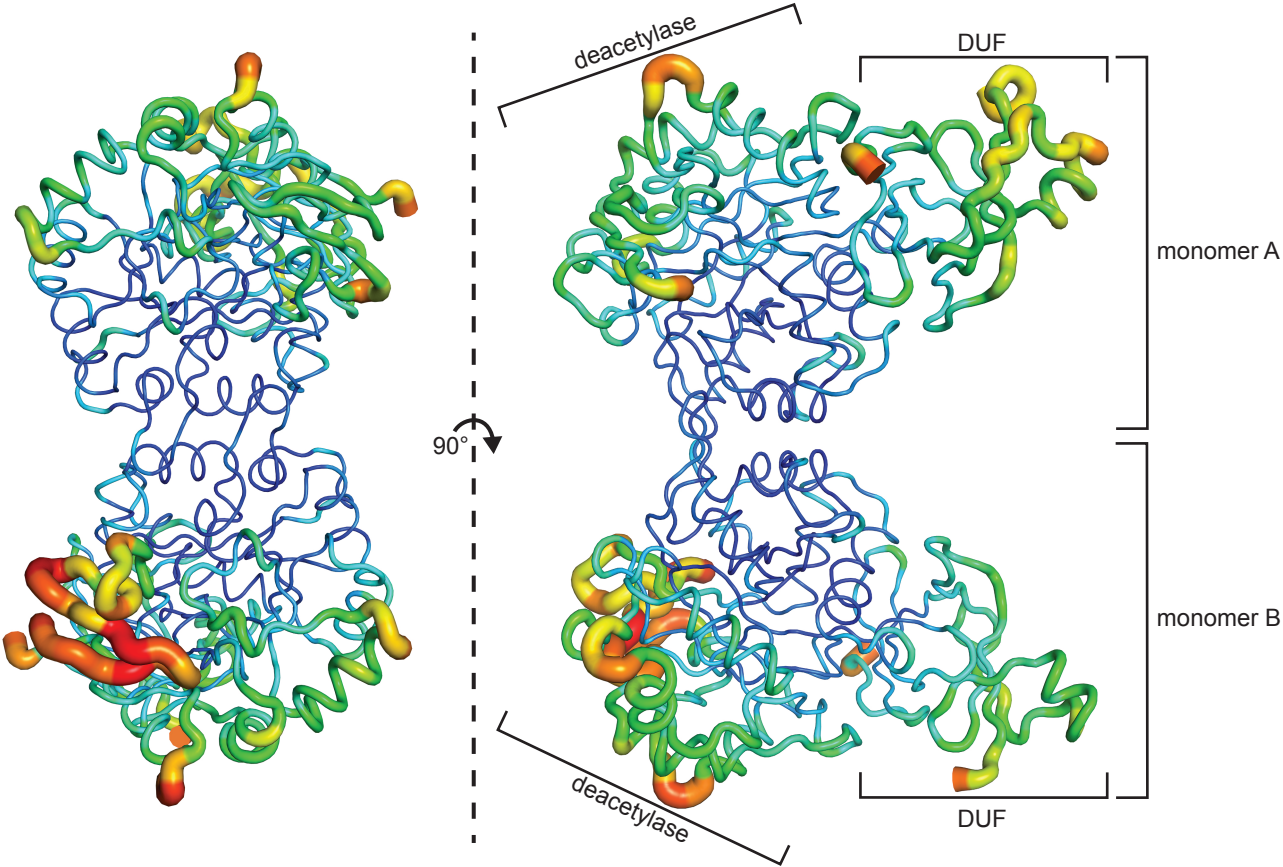


Figure 3-figure supplement 3

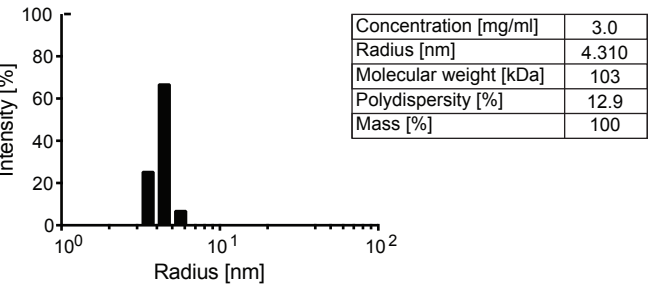


Figure 3-figure supplement 4

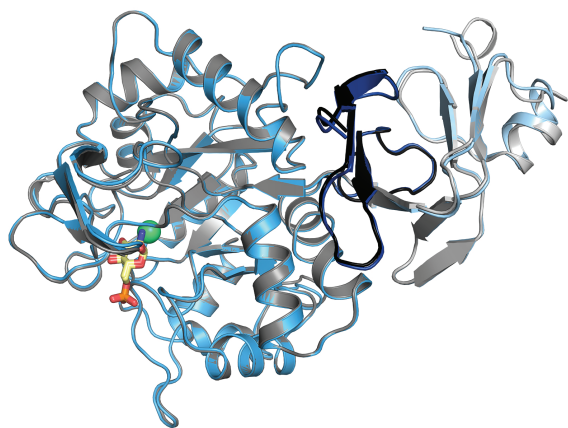


Figure 3-figure supplement 5

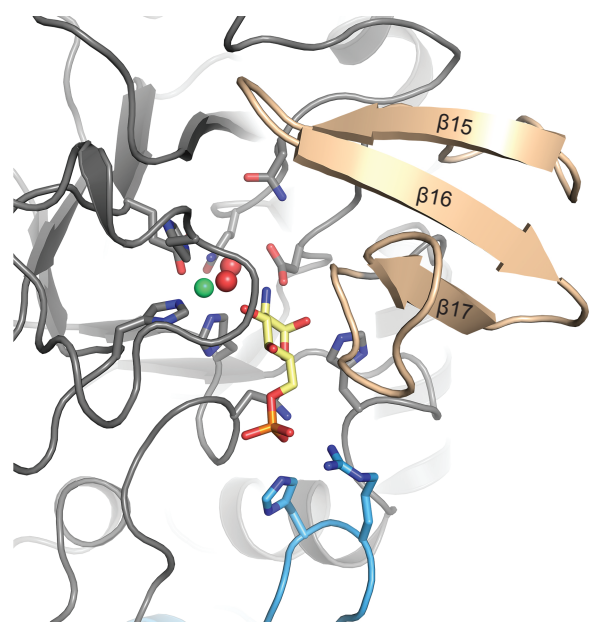


Figure 3-figure supplement 6

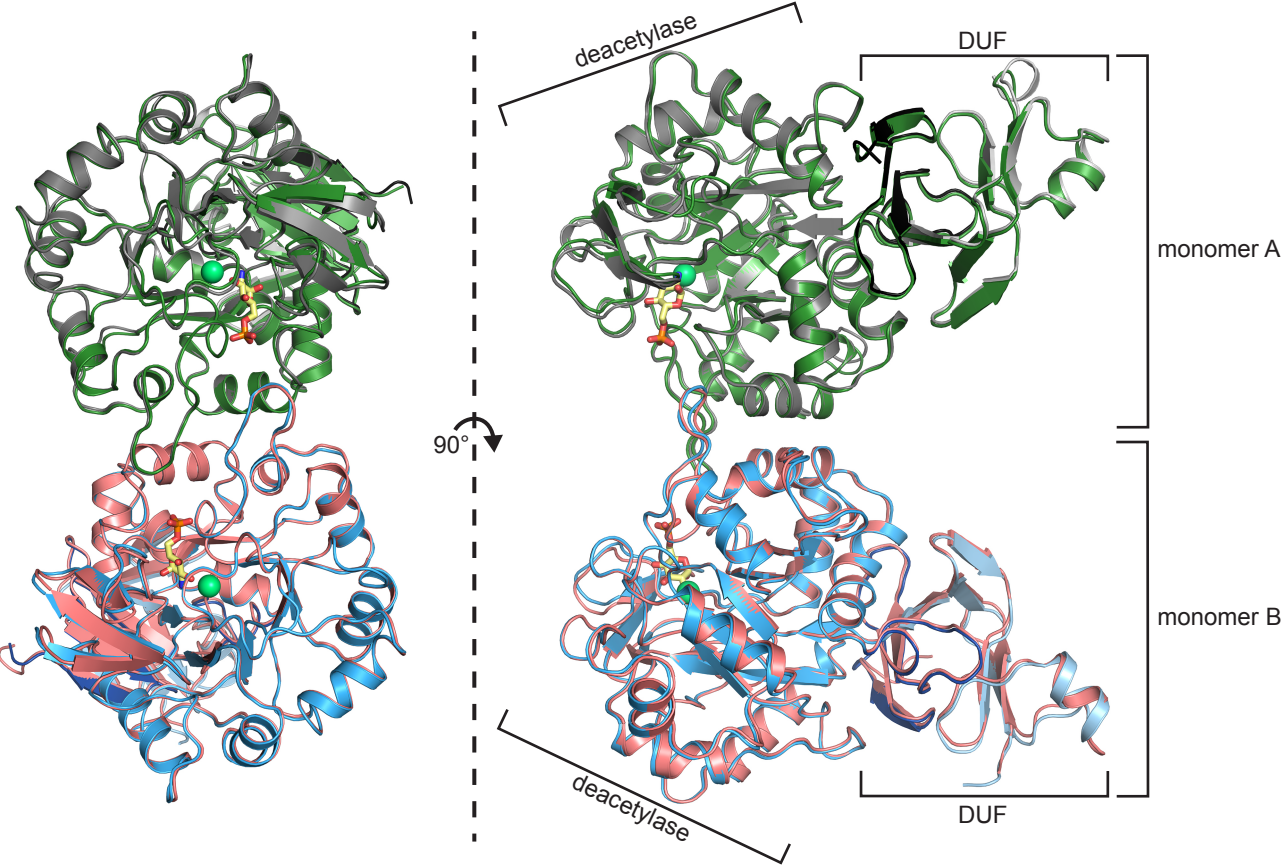


Figure 3-figure supplement 7

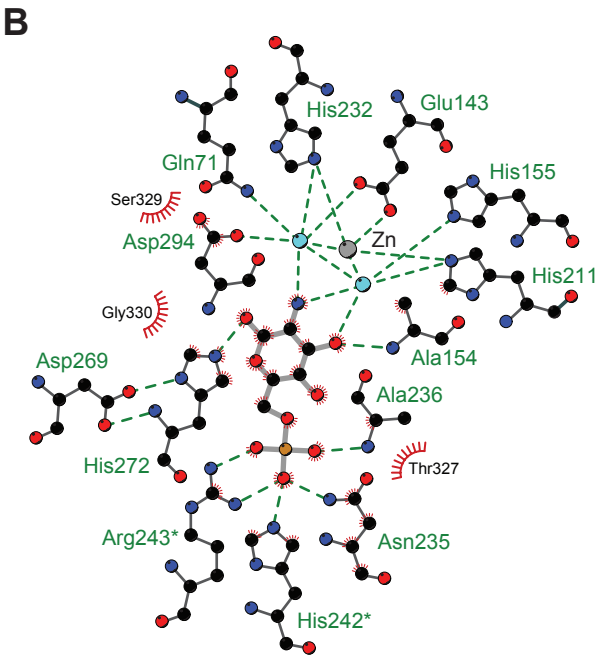
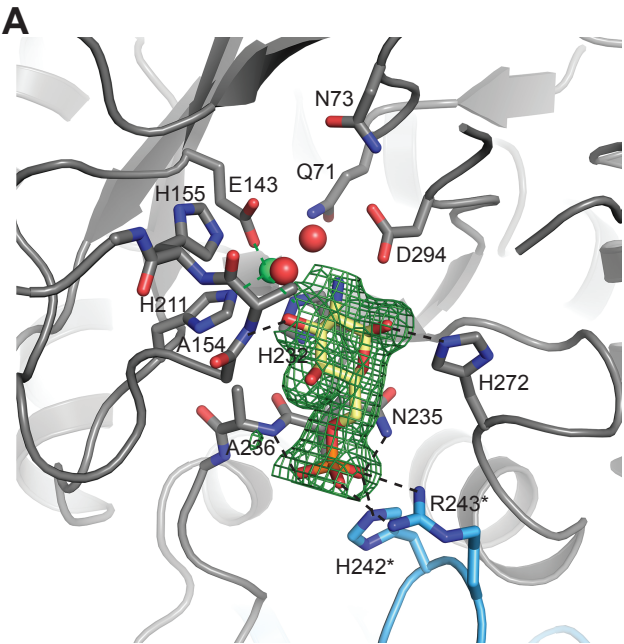


Figure 3-figure supplement 8

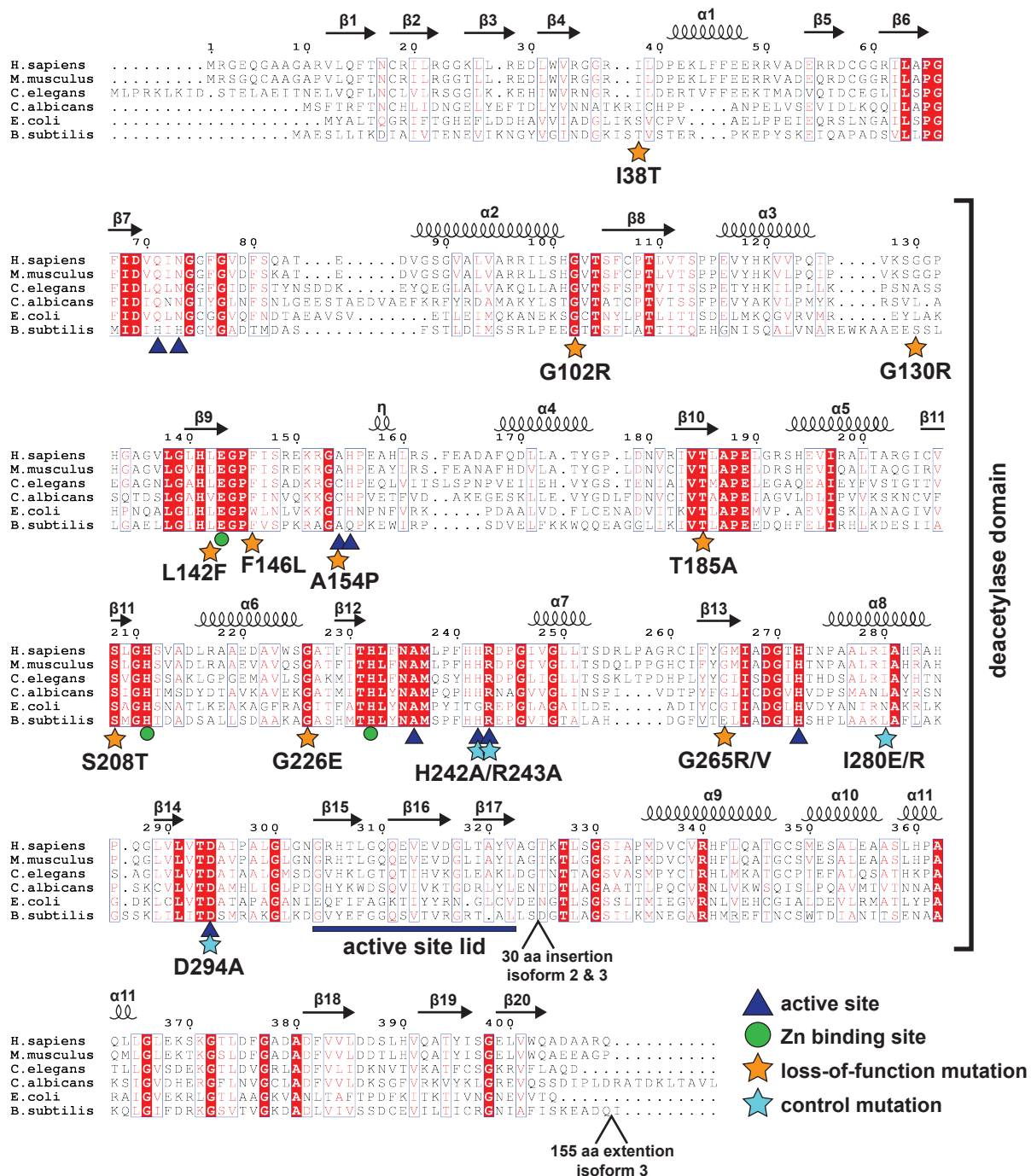


Figure 3-figure supplement 9

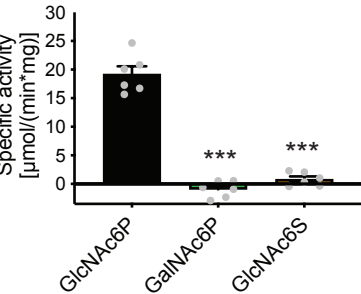


Figure 4-figure supplement 1

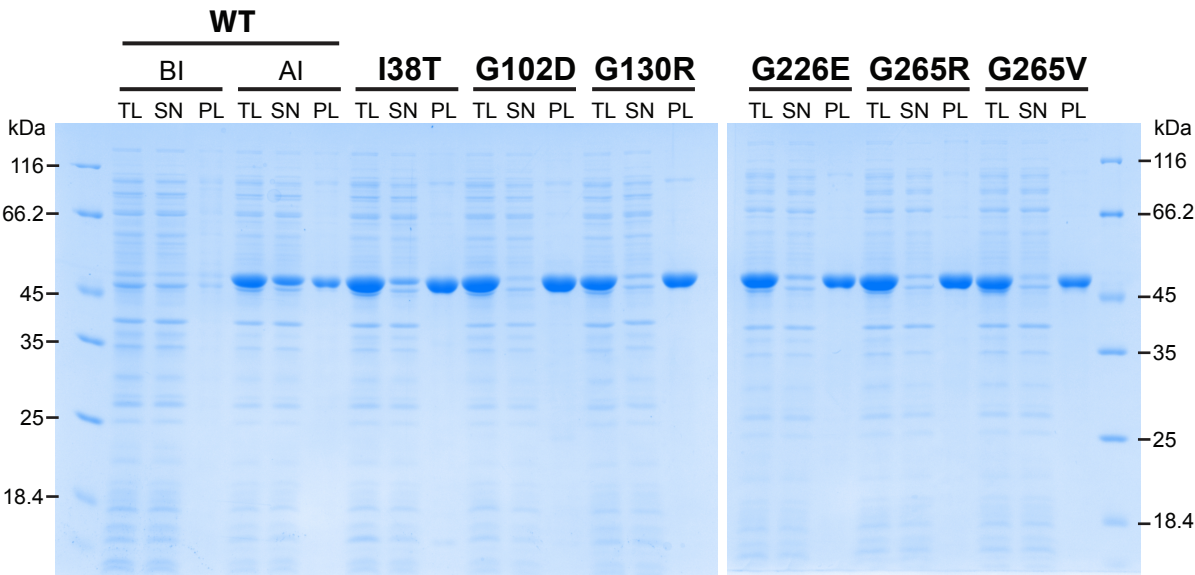


Figure 5-figure supplement 1

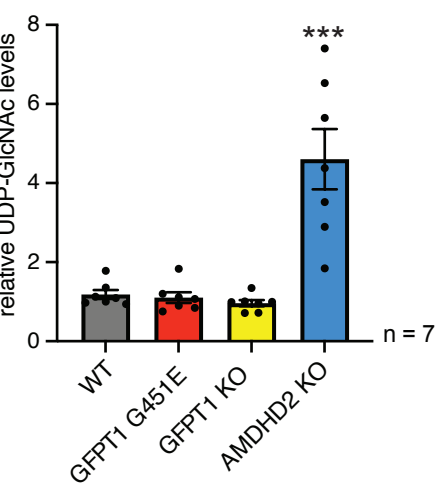


Figure 5-figure supplement 2

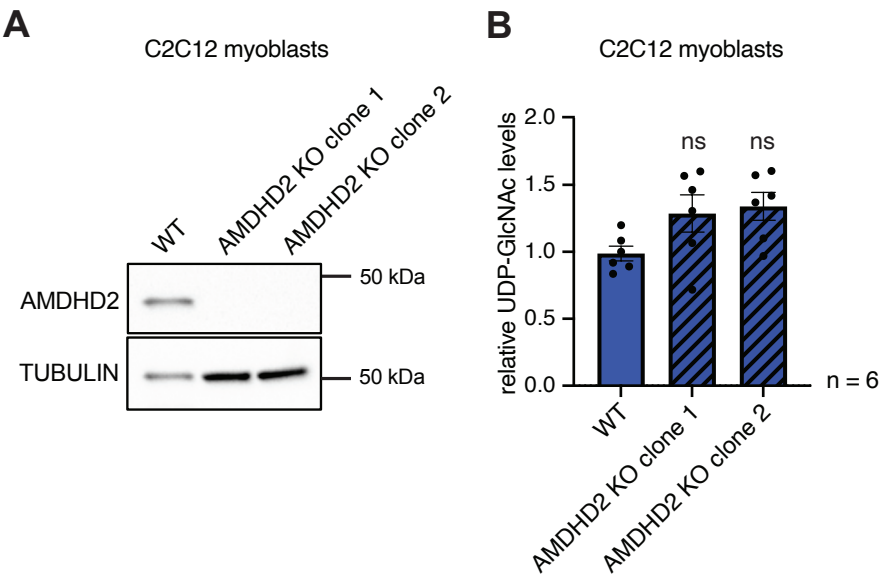


Figure 5-figure supplement 3

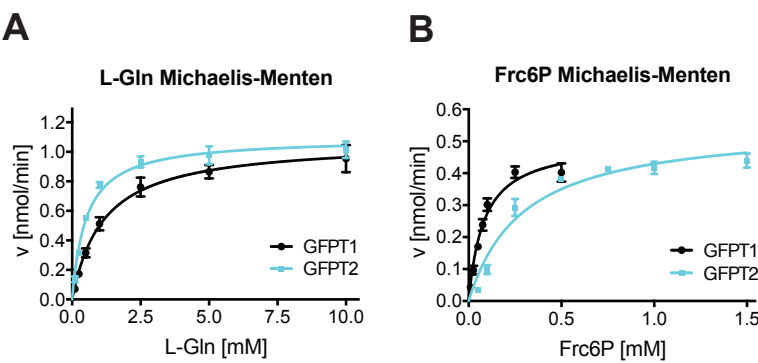


Figure 6-figure supplement 1

